

MICROCOPY RESOLUTION TEST CHART  
NATIONAL BUREAU OF STANDARDS-1963-A

# GROUND-BASED HIGH-POWER MICROWAVE DECOY DISCRIMINATION SYSTEM

AD-A189 311

Wilfried O. Eckhardt, Frank Chilton, Frank A. Dolezal, John I. Generosa, Robin J. Harvey,  
A. Jay Palmer, Gary A. Saenz, James G. Small, and Weldon S. Williamson

Hughes Research Laboratories  
3011 Malibu Canyon Road  
Malibu, California 90265

December 1987

Technical Progress Report No. 2  
Contract N00014-86-C-0878  
January 1, 1987 through December 31, 1987

Sponsored by:  
OFFICE OF NAVAL RESEARCH  
800 N. Quincy Street  
Arlington, VA 22217-5000

Monitored by:  
Dr. Howard E. Brandt  
Department of the Army  
Harry Diamond Laboratories  
2800 Power Mill Road  
Adelphi, MD 20783

**DTIC**  
**ELECTE**  
DEC 30 1987  
**S** **D**  
E

...has been approved  
...and sale; its  
distribution is unlimited.

REPORT DOCUMENTATION PAGE				Form Approved OMB No. 0704-0188	
1a. REPORT SECURITY CLASSIFICATION Unclassified		1b. RESTRICTIVE MARKINGS			
2a. SECURITY CLASSIFICATION AUTHORITY DoD Instruction No. 5210.72 (3/15/83)		3. DISTRIBUTION / AVAILABILITY OF REPORT			
2b. DECLASSIFICATION / DOWNGRADING SCHEDULE N/A					
3. PERFORMING ORGANIZATION REPORT NUMBER(S)		5. MONITORING ORGANIZATION REPORT NUMBER(S)			
5a. NAME OF PERFORMING ORGANIZATION Hughes Research Laboratories		6b. OFFICE SYMBOL (if applicable)	7a. NAME OF MONITORING ORGANIZATION Dr. Howard E. Brandt Department of the Army		
6c. ADDRESS (City, State, and ZIP Code) 3011 Malibu Canyon Road Malibu, CA 90265		7b. ADDRESS (City, State, and ZIP Code) Harry Diamond Laboratories 2800 Powder Mill Road Adelphi, MD 20783 SLCHD-NW-RA			
3a. NAME OF FUNDING / SPONSORING ORGANIZATION Office of Naval Research	8b. OFFICE SYMBOL (if applicable)	9. PROCUREMENT INSTRUMENT IDENTIFICATION NUMBER			
8c. ADDRESS (City, State, and ZIP Code) 800 N. Quincy Street Arlington, VA 22217-5000		10. SOURCE OF FUNDING NUMBERS			
		PROGRAM ELEMENT NO.	PROJECT NO.	TASK NO.	WORK UNIT ACCESSION NO.
11. TITLE (Include Security Classification) Ground-Based High-Power Microwave Decoy Discrimination System					
12. PERSONAL AUTHOR(S) W.O. Eckhardt					
13a. TYPE OF REPORT Technical Summary		13b. TIME COVERED FROM 1/1/87 to 12/31/87	14. DATE OF REPORT (Year, Month, Day) 1987 December 23		15. PAGE COUNT 99
16. SUPPLEMENTARY NOTATION					
7. COSATI CODES		18. SUBJECT TERMS (Continue on reverse if necessary and identify by block number)			
FIELD	GROUP	SUB-GROUP			
			Decoy Discrimination, High-Power Microwaves, Ballistic Missile Defense		
9. ABSTRACT (Continue on reverse if necessary and identify by block number)					
<p>The objectives of the subject contract are to conduct a detailed investigation of the feasibility of a ground-based high-power microwave decoy discrimination system, to explore key technology items required for the implementation of such a system, and to design a prototype system. If an effective defense against a massive strategic missile attack is to become feasible, one of the important problems that must be solved is to devise a system capable of reliable discrimination between decoys and reentry vehicles. In principle, high-power microwaves (HPMs) can be expected to provide an effective discrimination mechanism. The most important features of the concept are (1) all aspects of the system, with the possible exception of long-range sensors, are ground-based, yet there is an all-weather capability; (2) HPM/target interactions can be studied in ground-based experiments; and (3) the system hardware is expected to be highly modular and thus amenable to upgrading in several stages, based on successful testing.</p>					
20. DISTRIBUTION / AVAILABILITY OF ABSTRACT <input checked="" type="checkbox"/> UNCLASSIFIED/UNLIMITED <input type="checkbox"/> SAME AS RPT <input type="checkbox"/> DTIC USERS			21. ABSTRACT SECURITY CLASSIFICATION Unclassified		
2a. NAME OF RESPONSIBLE INDIVIDUAL W.O. Eckhardt		22b. TELEPHONE (Include Area Code) (213) 317-5253		22c. OFFICE SYMBOL	

19. (Continued)

The effort this year has again resulted in a considerably increased understanding of the critical issues affecting the feasibility of the proposed ground-based HPM decoy discrimination system. We have shown that the predicted damage mechanism can be produced in high vacuum, and that the experiments agree with the predictions of our HPM/target interaction model. We have proposed a mechanism that might enable the production of measurable thrust reactions from decoys with much thicker metal coatings than what was previously thought to be feasible. We have established bounds on some important parameters of the antenna system, and potential solutions to the single most critical problem - the cost of the large phased-array antenna - have been identified.

Accession For	
NTIS GRA&I	<input checked="" type="checkbox"/>
DTIC TAB	<input type="checkbox"/>
Unannounced	<input type="checkbox"/>
Justification	<i>per HP</i>
By _____	
Distribution/	
Availability Codes	
Dist	Avail and/or Special
<i>A-1</i>	



## TABLE OF CONTENTS

SECTION		PAGE
1	INTRODUCTION.....	1
2	DISCRIMINATION CONCEPT DESCRIPTION.....	5
	2.1 Approach.....	5
	2.2 Discrimination Mechanisms.....	8
	2.2.1 Changes in Optical and Microwave Signatures, Including Chaff Destruction.....	9
	2.2.2 Changes in Velocity Vector Caused by Vaporization Thrust.....	9
3	PROGRESS .....	11
	3.1 Tasks 1-3: Theoretical Study of HPM/Target Interactions.....	11
	3.1.1 Direct-Heating Model.....	12
	3.1.2 Electron-Bombardment Heating Model.....	18
	3.2 Tasks 4-6: Experimental Study of HPM/Target Interactions.....	27
	3.2.1 Experimental Apparatus.....	27
	3.2.2 Test Results.....	29
	3.2.3 Comparison with Analytical Model.....	34
	3.2.4 Limitations of Present Apparatus.....	34
	3.2.5 Planned Apparatus Revisions.....	36
	3.3 Task 7: Survey of the State of the Art in HPM Technology.....	38
	3.3.1 Virtual-Cathode (VC) Devices.....	39

SECTION	PAGE
3.3.2 Free-Electron Lasers (FELs) and Cyclotron Masers (CMs).....	41
3.3.3 Back-Wave Oscillators (BWOs).....	42
3.3.4 Cross-Field Oscillators/ Amplifiers (CFOs/CFAs).....	42
3.3.5 Cavity Compression.....	44
3.3.6 Summary.....	44
3.4 Tasks 8-10: System Design Study.....	45
3.4.1 Phased-Array Beam Steering and Focusing.....	45
3.4.2 The Effects of Aperture Thinning and Phase Errors on a Large Phased-Array Antenna.....	58
3.5 Tasks 17-18: High-Power Phase-Shifter Concept Exploration.....	70
3.5.1 Phase-Shifter Arrays.....	70
3.5.2 Magnetic Field Antennas.....	87
3.5.3 Electric Field Antennas.....	90
4 CONCLUSIONS .....	93
REFERENCES .....	95

## LIST OF ILLUSTRATIONS

FIGURE		PAGE
1	Ground-based HPM decoy discriminator.....	6
2	Ground-based HPM engagement ranges to midcourse targets.....	7
3	Microwave heating and thrusting of aluminized foils: theoretically modeled phenomena.....	13
4	Short-pulse theoretical results for aluminum....	17
5	Long-pulse theoretical results for aluminum.....	19
6	Experimental apparatus.....	28
7	Photograph of 12.5- $\mu\text{m}$ -thick Kapton sample with 10-nm-thick VDA coating, following 45-kW/cm <sup>2</sup> , 40- $\mu\text{s}$ HPM exposure.....	30
8	Photograph of 12.5- $\mu\text{m}$ -thick Kapton sample with 10-nm-thick VDA coating, following 44-kW/cm <sup>2</sup> , 40- $\mu\text{s}$ HPM exposure.....	31
9	Photograph of 12.5- $\mu\text{m}$ -thick Kapton sample with 20-nm-thick VDA coating, following 68-kW/cm <sup>2</sup> , 40- $\mu\text{s}$ HPM exposure.....	32
10	Photograph of 12.5- $\mu\text{m}$ -thick Kapton sample with 50-nm-thick VDA coating, following 42-kW/cm <sup>2</sup> , 40- $\mu\text{s}$ HPM exposure.....	33
11	Revised system.....	37
12	A single array element has a wide field of illumination.....	50
13	Extended arrays can form narrow beams when the contributions from each element arrive in phase at a distant point.....	51
14	The transmitted beam may be steered to the right by progressively phase shifting the discrete elements of the array.....	53

FIGURE		PAGE
15	For large ranges $R$ , converging spherical wavefronts differ from plane waves by less than $1/10$ wave over relatively large areas.....	57
16	Irradiance pattern for uniformly illuminated circular aperture.....	60
17	Irradiance pattern for centrally obscured circular aperture.....	62
18	Array of 64 small circular subapertures.....	63
19	Array of 16 circular subapertures.....	64
20	Far-field patterns of case A (diffraction-limited).....	65
21	Far-field patterns of case B ( $\lambda/40$ piston).....	67
22	Far-field patterns of case C ( $\lambda/20$ piston).....	68
23	Far-field patterns of case D ( $\lambda/10$ piston).....	69
24	Resonant loop.....	71
25	Array of resonant loops.....	71
26	Phase shift in reflection.....	72
27	Loop in B-field.....	75
28	Voltage-driven loop.....	75
29	Magnetic moment of loop.....	77
30	Scattered dipole field.....	78
31	Sheet of magnetic dipoles.....	80
32	A ring of dipoles.....	80
33	Scattering by dipole sheet.....	83
34	Delay by dielectric layer.....	83
35	Resonant loop dimensions.....	86
36	Single-turn resonator.....	87

**FIGURE**

**PAGE**

37	The 2-band halo antenna.....	89
38	Dipole phase-shifter arrays.....	91
39	Dipole tuning methods.....	92
40	Digitally switched reflecting arrays.....	92

## SECTION 1

### INTRODUCTION

The objectives of the subject contract are to conduct a detailed investigation of the feasibility of a ground-based high-power microwave decoy discrimination system, to explore key technology items required for the implementation of such a system, and to design a prototype system. If an effective defense against a massive strategic missile attack is to become feasible, one of the important problems that must be solved is how to devise a system that is capable of reliable discrimination between decoys and reentry vehicles (RVs). The following discussion shows that, in principle, high-power microwaves (HPM) can be expected to provide such a discrimination mechanism.

Estimates of the transmitter power, antenna size, and other pertinent requirements for a ground-based HPM system capable of performing the discrimination function have shown that the required parameter values are reasonable. The most important features of the proposed concept are that all assets of the system, with the possible exception of long-range sensors, be ground-based, yet that there is an all-weather capability; that HPM/target interactions can be studied in ground-based experiments; and that the system hardware is expected to be highly modular and thus amenable to upgrading in several stages, based on successful testing.

The technical monitor for the subject contract is Dr. Howard E. Brandt, OSD/SDIO-IST and Harry Diamond Laboratories. The contract effort is being performed at Hughes Research Laboratories (HRL), Malibu, CA; at the Albuquerque Engineering Laboratory (AEL) of the Hughes Aircraft Company Electro-Optical and Data Systems Group; by Hughes Aircraft consultant Dr. Frank Chilton; and under subcontract by Dr. John I. Generosa of Physical Research, Inc., Albuquerque, NM. Overall program

management responsibility is assigned to Dr. Wilfried O. Eckhardt, Senior Scientist in the Plasma Physics Department of HRL, whose Manager is Dr. Jay Hyman. Dr. James G. Small, Senior Scientist in the AEL, has responsibility for the program elements residing at Albuquerque. Dr. Chilton is in charge of several of the theoretical tasks. Dr. Generosa conducts the survey of the state of the art in HPM technology. Other contributors at HRL are: Franklin A. Dolezal; Dr. Robin J. Harvey, Senior Scientist and Section Head in the Plasma Physics Department; Dr. A. Jay Palmer; Dr. Gary A. Saenz; and Dr. Weldon S. Williamson.

This report covers the second period of funding under the subject contract. Our effort this year was concentrated on the following tasks (as listed in the Contract Task Breakdown shown in Technical Progress Report No. 1):

**Tasks 1-3: THEORETICAL STUDY OF HPM/TARGET INTERACTIONS**

The contractor shall complete a theoretical analysis of HPM/target interactions.

**Tasks 4-6: EXPERIMENTAL STUDY OF HPM/TARGET INTERACTIONS**

The contractor shall perform an experimental study of HPM/target interactions and shall perform measurements of potential HPM discrimination mechanisms. The experiments are to uniquely address the physical-damage mechanisms and decoy signature modifications possible through HPM irradiation.

**Task 7: SURVEY OF THE STATE OF THE ART IN HPM TECHNOLOGY**

The contractor shall perform a continuous survey of the state of the art in HPM technology and identify and document developments which could be critical to the feasibility of a ground-based discrimination system and its possible countermeasures. Special attention shall focus on HPM oscillator and amplifier technology.

Tasks 8-10: SYSTEM DESIGN STUDY

The contractor shall complete a conceptual design study of an overall decoy discrimination system.

Tasks 17-18: HIGH-POWER PHASE-SHIFTER CONCEPT EXPLORATION

The contractor shall investigate the feasibility of HPM phase shifters to be used in HPM phased arrays.

As a reminder of the overall approach, we repeat as Section 2 of this report the Discrimination Concept Description from Technical Progress Report No. 1. We have shown this year that the predicted damage mechanism can be produced in high vacuum, and that the experiments agree with the predictions of our HPM/target interaction model. Also, potential solutions to the single most critical problem - the cost of the large phased array - have been identified.

## SECTION 2

### DISCRIMINATION CONCEPT DESCRIPTION

#### 2.1 APPROACH

The midcourse scenario is likely to include hundreds of balloon-like decoys for each RV. Effective decoys must be indistinguishable from RVs to all the sensors that can challenge them. More precisely, considering the realities of the situation, the RVs must be camouflaged so they are indistinguishable from the decoys.

The system being investigated here would employ a ground-based HPM system to modify by a physical damage mechanism, during midcourse flight, one or more of those characteristics of decoys (and decoy-camouflaged RVs) that are readily observable by microwave and optical radars. One of the requirements of this system is that it avoid air breakdown (at the Paschen minimum occurring at an altitude of about 50 km) while placing a sufficient power density on target; this appears to be quite feasible.

Figure 1 shows schematically how the proposed HPM system would irradiate a decoy-camouflaged RV that is surrounded by a cluster of decoys. Figure 2 shows typical engagement ranges to mid-course targets for such a system.

It is possible, of course, to design decoys that the proposed system cannot modify sufficiently to render them distinguishable from RVs by microwave and optical radars. In this case also, a major military objective has been realized, since such decoys must be significantly heavier and more complex (and therefore significantly fewer in number) than decoys designed to respond only to nonintrusive probing by microwave and optical radars.

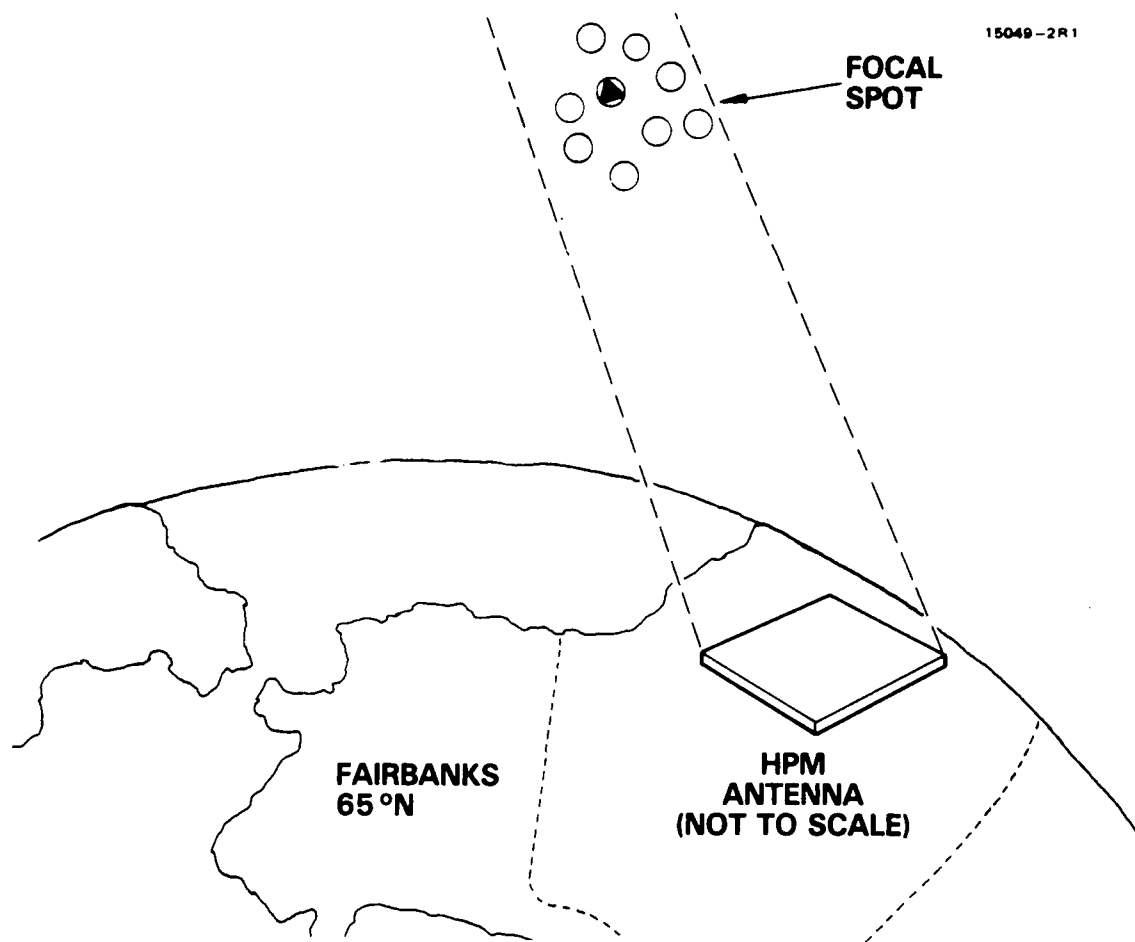


Figure 1. Ground-based HPM decoy discriminator.

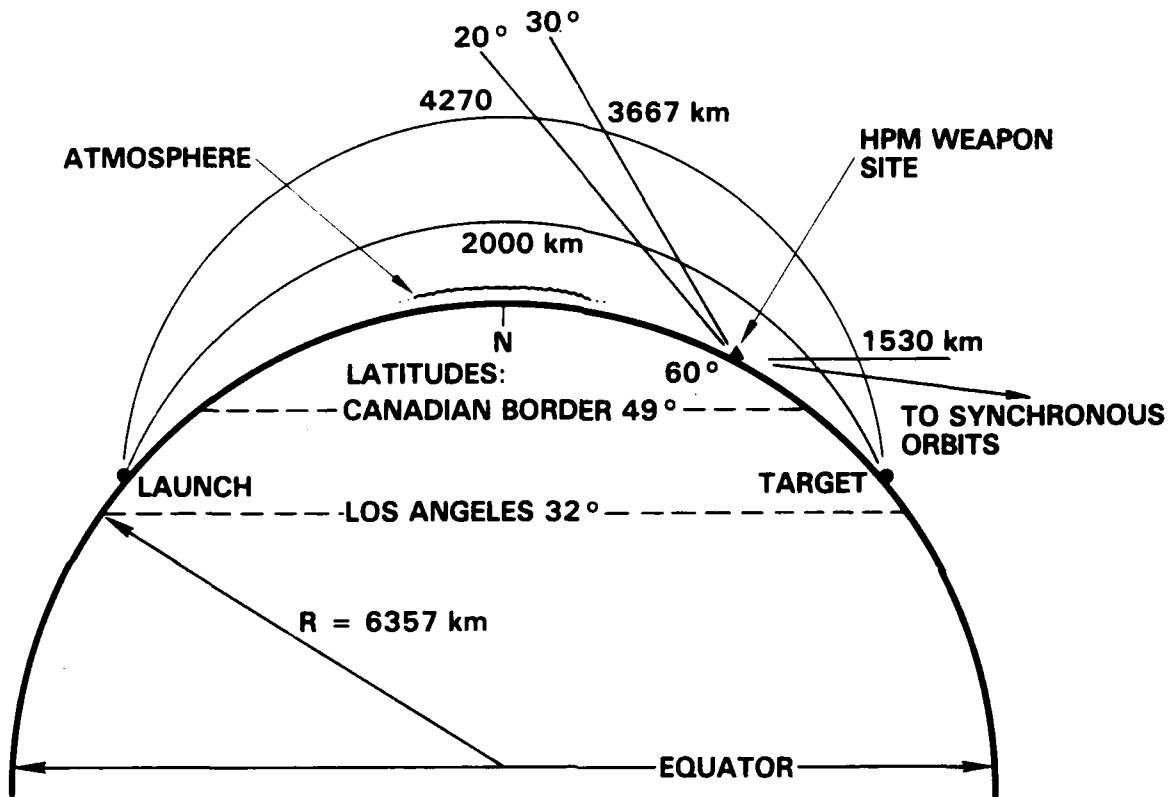


Figure 2. Ground-based HPM engagement ranges to midcourse targets.

## 2.2 DISCRIMINATION MECHANISMS

Thin metallic films are used on optical surfaces (e.g., focusing mirrors and corner reflectors), on glass and plastic fibers for radar chaff, and probably as the outer (and/or inner) coating of metalized plastic decoy balloons. Very-high-power microwave fields can interact in a strongly nonlinear fashion with such metal films. Because of their finite conductivity, the films are less than perfect reflectors and will absorb some of the incident microwave power; this is especially significant when the film thickness is less than the skin depth at the applied microwave frequency. Under these conditions, and at sufficiently high incident pulse energy density levels, metal films can be vaporized by ohmic heating.

The threshold energy density required for film evaporation is minimized by using short pulses. Concentrating a given pulse energy in short pulses prevents the possibility that an appreciable fraction of the generated heat energy could be conducted into the plastic substrate of the metal film before film evaporation is completed.

Given that sources capable of producing the described effect are practical, at least the following two discrimination methods might be exploited for nonintrusive probing by microwave and optical radars after the objects in question have been subjected to HPM irradiation. (Note that a ground-based HPM system could, in principle, also provide the nonintrusive probing function by operating in both high-power and low-power modes: at low power levels, it would operate as a conventional phase-steered radar to acquire and track targets; high-power pulses to modify the targets would be followed by low-power pulses to assess changes in target signatures).

### 2.2.1 Changes in Optical and Microwave Signatures, Including Chaff Destruction

Vaporization of metal films from plastic balloons and other surfaces would produce permanent changes to both the microwave and optical radar signatures of decoys and decoy-camouflaged RVs. Specifically, the balloons would become sufficiently transparent to the probing radiation that an RV hidden inside would be readily discernible. An alternative damage mechanism is melting of the plastic substrate, since the metal films are so thin.

In addition to being subject to thin-film damage, decoys will be particularly vulnerable to HPM irradiation at joints, seams, and wire attachment points where electric fields or currents are concentrated. (For example, localized sparking is readily observed on aluminum-foil-covered objects placed in microwave ovens.) Multiple high-energy pulses can be expected to cause progressive or catastrophic structural failure in low-mass decoys.

We anticipate that a finely dispersed cloud of radar chaff will accompany RV and decoy clusters as a countermeasure against radar discrimination. Radar chaff consists of metal-coated glass or plastic fibers. Fibers on the order of half a wavelength long are strong reflectors. A ground-based HPM system could evaporate the chaff coatings or melt the fibers into little balls. Several pulses would probably be required to couple to the various orientations of slowly rotating fibers. HPM irradiation could also evaporate the metal coatings on optical corner reflectors, which serve the analogous function of optical chaff to laser radars.

### 2.2.2 Changes in Velocity Vector Caused by Vaporization Thrust

Vaporization of a metal film from the decoy surface could produce a sufficient thrust to cause a detectable velocity change in low-mass decoys. If sufficient energy densities are conducted and radiated by a metal film into its plastic substrate as the metal vaporizes, the plastic material could also partially vaporize or ablate and thereby increase the resulting thrust.

## SECTION 3

### PROGRESS

The progress achieved during the period of performance from 1 January to 31 December 1987 is reported in accordance with the Contract Task Breakdown shown in Technical Progress Report No. 1.

#### 3.1 TASKS 1 - 3: THEORETICAL STUDY OF HPM/TARGET INTERACTIONS

The theoretical treatment of the expected HPM/target interactions as described in Section 2.1.2 of the proposal leading to this contract contains a number of approximations and assumptions that are valid for an order-of-magnitude estimation of the required system performance parameters. We have now performed a much more refined analysis of the interaction of HPM pulses with metal layers and substrates, and have thus obtained a correspondingly more precise prediction for the performance-parameter requirements. This analysis ("Direct-Heating Model") is described in Section 3.1.1 below. It is gratifying to note that the new theoretical results deviate by only 20% (in the beneficial direction) from the predictions based on the approximative model. Both of these theoretical models are conservative in that they ignore any enhancements of the HPM/target interaction that may result from the presence of charged particles adjacent to the target surface.

For decoys with thick metal coatings, this conservative theoretical treatment does not predict HPM/target interaction effects that are useful for decoy discrimination. The prospects appear very different, however, when plasma effects are taken into account. An outline for the theoretical treatment of the expected effects ("Electron-Bombardment Heating Model") is described in Section 3.1.2.

### 3.1.1 Direct-Heating Model

During this contract period, we have developed a detailed theoretical model for the coupling of high-power microwave radiation to a metallized foil. The model is currently capable of predicting the temperature rise of a metallized dielectric substrate as a function of time and distance into the foil. The model also computes the vaporization rate of the irradiated surface and the associated recoil velocity of the foil due to vaporization blow-off. These phenomena are depicted in Figure 3.

In addition to the spatial and temporal variations, other key ingredients of this model that were not included in our earlier preliminary models of HPM heating are the use of temperature-dependent (rather than average) specific heat and conductivities, and the inclusion of internal reflections of the microwave radiation within the metalization layer. Inclusion of this latter phenomenon in the model leads to much higher predicted heating rates than were obtained earlier<sup>1</sup> when the thickness of the aluminum layer is comparable to or less than the skin depth.

After the onset of vaporization, the metal thickness is also a time-dependent variable in the model. This is important because the effective transmission of the microwave flux into the metal depends sensitively on the thickness because of the multiple reflections within the metal.

Finally, all important heat losses are accounted for. These include: radiation and vaporization, and thermal diffusion through both the metal and the substrate.

The primary assumptions of the model are that it is one-dimensional and that the vaporization of the metal occurs at the sea-level boiling point which is about 2,600 °K for aluminum.<sup>2</sup> This latter assumption is justified by the exponential rise of the vapor pressure with temperature near the boiling point. During vaporization we neglect radiative and conductive losses compared with the much larger vaporization energy loss.

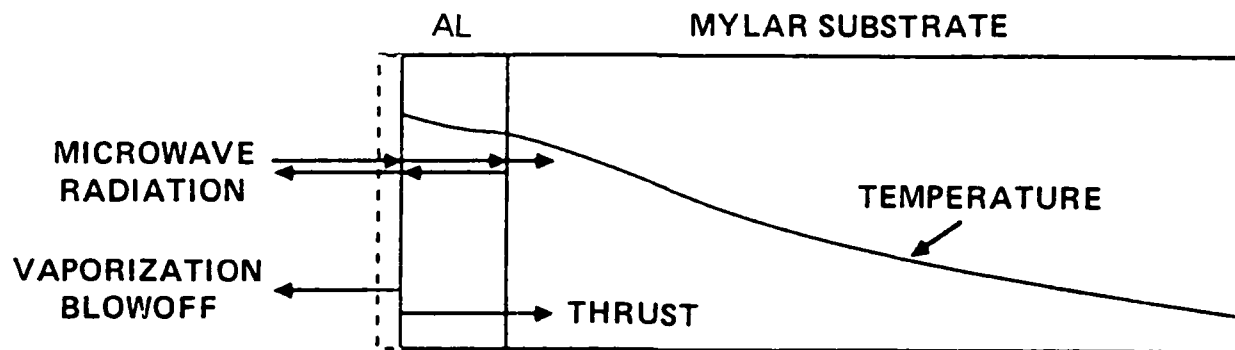


Figure 3. Microwave heating and thrusting of aluminized foils: theoretically modeled phenomena.

Governing Equations. The fundamental equation for the model is the heat balance equation for the metallized layer:

$$\partial T / \partial t = (1 / \rho C) [\sigma TR E^2 - K \partial^2 T / \partial z^2 - 2\epsilon(T_S^4 - T_0^4) / L], \quad (1)$$

where E is the peak electric field amplitude of the incident microwave radiation, TR is the transmission coefficient of the radiation into the metal, C is the specific heat,  $\sigma$  is the electrical conductivity, K is the thermal conductivity,  $\epsilon$  is the emmissivity,  $\rho$  is the density,  $T_0$  is the initial temperature, L is the thickness of the metal layer, and  $T_S$  is an effective surface temperature for the layer. This fully spatially dependent thermal diffusion equation was solved numerically to confirm that for pulse lengths longer than a small fraction of a nanosecond, aluminized layers whose thickness is on the order of a micron or less are heated uniformly. In this case we may set  $T_S = T$ , and we need only compute the thermal conduction term in the substrate material.

For use in Eq. (1), tabulated data for the temperature-dependent specific heat and thermal conductivity of aluminum were obtained from Refs. (3) and (4), respectively. The temperature dependence of the electrical conductivity was obtained by applying the Wiedemann-Franz law<sup>5</sup> to the thermal conductivity. The specific heat and thermal conductivity values for the substrate (Mylar) were assumed to be constant and were obtained from Ref. (6).

The transmission coefficient into the aluminum layer, TR, was obtained by applying the continuity condition for the tangential electric field component across the surface of incidence to the reflectivity formula for a thin film.<sup>7</sup> We obtain:

$$TR = \left| \frac{1 - r[1 - \exp(2ik_m L)]}{[1 - r^2 \exp(2ik_m L)]} \right|^2, \quad (2)$$

where  $k_m = \delta^{-1}(1+i)$ ,  $\delta$  is the skin depth, and

$$r = (k_0 - k_m) / (k_0 + k_m) , \quad (3)$$

where  $k_0$  is the free-space wavenumber of the radiation.

In the results presented below, once the temperature reaches the sea-level boiling point (2,600 °K for aluminum),<sup>2</sup> the temperature is held constant while the foil thickness is reduced as a result of vaporization of the irradiated surface at a rate given by:

$$dL/dt = - v_s , \quad (4)$$

where the surface velocity  $v_s$  is given by conservation of energy<sup>8</sup>:

$$\int (\sigma TR E^2) dz = v_s \rho (C T_v + h_v) , \quad (5)$$

where  $T_v$  is the vaporization temperature,  $h_v$  is the heat of vaporization, and the integral is through the foil thickness  $L$ .

Finally, the recoil velocity of the foil due to the vaporization blow-off is computed by invoking conservation of momentum:

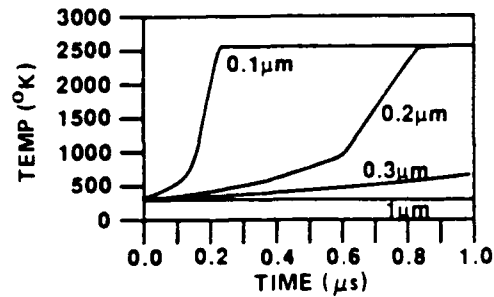
$$\frac{d}{dt} (v_{\text{thrust}}) = v_s v_b \rho / (\rho L + \rho_s L_s) , \quad (6)$$

where s-subscripts refer to substrate, and  $v_b$  is blow-off velocity, assumed equal to the thermal velocity of the vapor at the vaporization temperature.

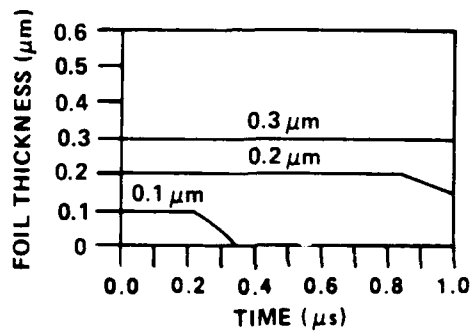
The model neglects the coupling of the radiation to the vapor being expelled from the foil and to any ambient vapor. In order for the vapor to significantly increase the heating or vaporization of the foil, the energy deposition rate per unit volume in the vapor would need to be greater than or comparable to that in the foil. The maximum energy deposition rate per unit volume in the vapor occurs when the plasma frequency and the collision frequency have become equal to the radiation frequency.<sup>9</sup> Under this condition, the attenuation distance in the vapor is on the order of a radiation wavelength. It turns out that a 0.1- $\mu\text{m}$  foil has just enough material to fill this wavelength-thick layer at a vapor density ( $\sim 10^{17} \text{ cm}^{-3}$ ) which satisfies the above collision frequency criterion. The plasma frequency can easily become on the order of the radiation frequency requiring an electron density of only  $\sim 10^{12} \text{ cm}^{-3}$ . But, even if these conditions do occur, the energy deposition per unit volume in the vapor will be about three orders of magnitude less than that in the foil. Therefore, the neglect of radiation heating of the vapor appears to be justified for calculating vaporization rates of metallized foils.

On the other hand, the presence of a plasma adjacent to the irradiated surface could also lead to a significant reduction of heating due to added reflection from the plasma layer when plasma frequencies become comparable or larger than the microwave frequency. Therefore, the development of a plasma layer in the blow-off layer will be assessed in a more complete treatment of the vaporization and thrusting of metallized foils by high-power microwaves (see also Section 3.1.2).

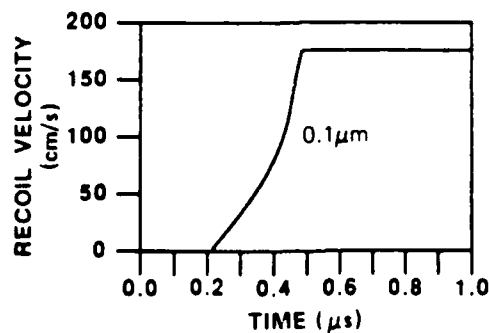
Theoretical Results. In Figure 4 are shown the predicted temperature, foil thickness, and recoil velocity versus time for the high-power, short-pulse microwave irradiation of aluminized Mylar at levels comparable to what might be achievable from a large-scale microwave transmitter array.



(a)



(b)



(c)

Figure 4. Short-pulse theoretical results for aluminum (parameter: original layer thickness) on a 250- $\mu\text{m}$  Mylar substrate irradiated by 10-GHz radiation at 30  $\text{MW}/\text{cm}^2$ : (a) temperature versus time, (b) aluminum thickness versus time, (c) recoil velocity versus time.

The parameter on which the heating rate depends most sensitively in this regime is the initial aluminum layer thickness. This is because of the rapid reduction of the transmission coefficient of the microwave energy into the aluminum as the layer thickness is increased towards the skin depth. For the 10-GHz, 1- $\mu$ s, 30-MW/cm<sup>2</sup> irradiation levels chosen for these examples, it is seen that significant vaporization and thrusting will occur only for an aluminized layer thickness at or below about 0.1  $\mu$ m.

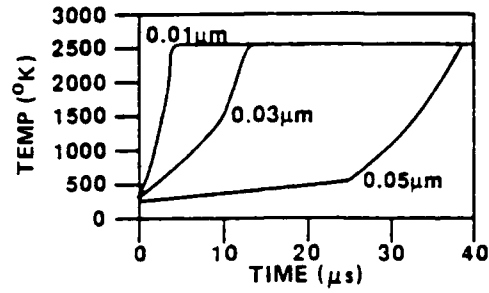
Figure 5 shows additional theoretical results. These results are for the lower-power, longer-pulse-length microwave irradiation levels used in the laboratory experiments. Here, the results for the foil thickness reduction in Figure 5(b) are consistent with what was observed in the experiments, giving us confidence in the validity of the theoretical model we have constructed.

### 3.1.2 Electron-Bombardment Heating Model

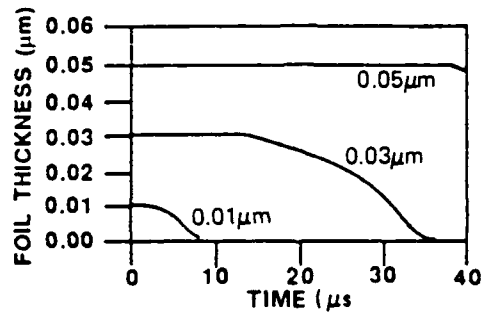
This section treats the search for other mechanisms than direct heating. The mechanisms researched were then pursued in proportion to their likelihood of use in decoy discrimination. The objectives were to investigate phenomena, other than direct heating, which can cause:

- Demetallization
- Changes in velocity
- Changes in radar cross section
- Other signatures

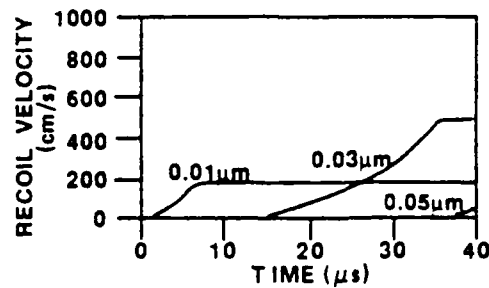
The limitation on direct heating results from the high reflectance of metals, so direct heating produces demetallization of thin films, but not thick films. However, we have noticed that when air was present due to poor vacuum, micron-thick aluminum films were easily removable. Further there usually is



(a)



(b)



(c)

Figure 5. Long-pulse theoretical results for aluminum (parameter: original layer thickness) on a 25- $\mu\text{m}$  Mylar substrate irradiated by 4-GHz radiation at 44  $\text{kW}/\text{cm}^2$ : (a) temperature versus time, (b) aluminum thickness versus time, (c) recoil velocity versus time.

some arcing, balloon popping, etc. These observations suggest that plasma effects would be important in vacuum, if there are mechanisms which will produce plasma. Plasma enhancement is well known in sputtering and etching technologies (Refs. 10-12).

It is certainly not surprising that plasma phenomena would become important when one considers the maximum expected power density of 30 MW/cm<sup>2</sup> at range. That is about a factor of 10 above the power density that passes through a vacuum waveguide without excessive arcing, which quickly ruins the waveguide. And the metal on decoys cannot be treated and finished, as waveguide can, without destroying the metal film and plastic substrate. The free-wave electric field strength is about 100 kV/cm (rms). This is comparable to the dielectric strength of the polymer substrate on balloon decoys (Ref. 13).

Philosophically, we tried to keep an open mind in the search for other mechanisms because this range of microwave power densities is above that with which anyone has direct experience, so analogies to other regions of experience are important. Table 1 presents the long list of phenomena which could be relevant and therefore must be considered and evaluated. We are especially looking for effects that become important at high field strengths, power, and energy densities.

TABLE 1. Relevant Phenomena

- Arcs and Sparks
- Thermionic Emission
- Field Emission
- Secondary Emission
- Electron and Ion Impact Phenomena
- Sputtering
- Plasma Etching
- Plasma Phenomena
- Demetallization
- Electron Bombardment Phenomena

Sputtering and plasma etching looked promising at first but there appeared to be no plausible source of ions to begin the process. A second difficulty was the frequency range, which to optimize antenna gain had to be too high by  $10^3$  for optimum sputtering and etching.

Recently, a more promising direction for research resulted from noticing that our microwave power density was greater or comparable to the electron power densities in electron beam evaporation and welding technology. Thus, if the microwave power were transferred to an electron plasma, then that electron plasma could transfer energy to the surface and demetallize it, at least partially, even if the films are thick. The question is whether sufficient energy density is transferred to the electron plasma to cause demetallization by electron bombardment.

To construct a theoretical model of transfer of power through an electron plasma, the initial approach is summarized in Table 2. This model is now at the simplest level, a kinetic theoretic approach using average values. This approach was used in order to quickly evaluate whether this model was promising for further study.

First there need to be a few seed electrons. These can arise from many mechanisms such as thermionic emission from the direct heating or sunlight, photoemission from energetic photons from the sun, or field emission from the high field strengths, when enhanced by geometry or surface ions (arcs, etc.). Since about 1 electron/cm<sup>3</sup> is enough, seed electrons are assured.

As stated above, the power density of 30 MW/cm<sup>2</sup> corresponds to a free-wave electric field  $E_0 \approx 100$  kV/cm (only two significant figures will be kept in these estimates to remind us that they are estimates). The next task is to compute average values of the electric field. If we imagine the target to be a sphere then, choosing normal incidence as the pole, the incident electric field is parallel at the pole, and for linear

TABLE 2. Electron-Bombardment Model.

- Arcs and/or thermionic emission cause a few seed electrons.
- Electrons within the  $\sim 0.5$ -mm sheath which can hit the surface bombard the surface every other half cycle where  $E_n \gg 0$ .
- Secondary emission causes exponential growth,  $\exp(Sft)$ , where  $S \approx 0.5$  for metals at high impact energies. ( $1+S$  is the conventional secondary emission coefficient.)
- The electron plasma continues to grow to a little above critical  $n \approx 10^{14} \text{cm}^{-3}$ , since it is thin compared to a skin depth.
- The plasma is trapped near the surface by pondermotive and electrostatic forces.
- Is there some value of  $n$  for which the transfer of energy from microwaves to surface heating is nearly complete?
- At  $n \approx 10^{14} \text{cm}^{-3}$  most of the incident energy is transferred to the surface by electron bombardment, causing demetallization.
- Since electron energies exceed 1 keV, some ion involvement should occur in the later stages of development of the plasma.
- The electrostatic sheath should also increase ion bombardment in the later stages, just as it helps in sputtering.

polarization completely normal on the equator at two points 180° apart. At 90° from those two points the linear polarization causes the incident field to be all parallel. This fixes the geometry.

Near the surface of a thick metal, to a part in  $10^{-4}$ , the boundary conditions cause a doubling of  $E_n$  and  $H_{||}$  due to surface charges and currents, and a cancelling of  $E_{||}$  and  $B_n$ . These surface charges and currents flow over a depth scale of order the skin depth, about 1  $\mu\text{m}$ , and the depth scale of plasma effects will be much greater.

Thus the mean square value of the normal electric field including E-doubling, spatial averaging over a hemisphere, and time averaging is

$$\overline{E_n^2} = \frac{1}{2} \times 4 E_o^2 \int_0^1 d\cos\theta \int_0^{2\pi} \frac{d\phi}{2\pi} \sin^2\theta \cos^2\phi = \frac{2}{3} E_o^2, \quad (7)$$

and the average (rms) field over the entire exposed hemisphere is

$$E_a \equiv \overline{E_n^2}^{1/2} \approx 82 \text{ kV/cm} = 8.2 \text{ MV/m}, \quad (8)$$

which is also quite high. Incidentally, the average field for other shapes would be of the same order of magnitude.

The electrons will undergo simple harmonic motion due to  $E_n$ . We need to estimate the average thickness of the sheath which can bombard the surface and the average energy of those electrons. From Newton's law,

$$m \frac{d^2x}{dt^2} = eE, \quad (9)$$

the mean square displacement  $x$  and velocity  $v$  are

$$\overline{x^2} = \left| \frac{eE_a}{m\omega^2} \right|^2 \quad \text{and} \quad (10)$$

$$\overline{v^2} = \left| \frac{eE_a}{m\omega} \right|^2$$

since  $E_a$  includes a time averaging already which, with  $e = 1.6 \times 10^{-19}$  C,  $m = 9.1 \times 10^{-31}$  kg,  $\omega = 2\pi f$ ,  $f = 10^{10}$  Hz, yields

$$x_a \equiv \overline{x^2}^{1/2} = 0.37 \text{ mm} \quad (11)$$

and

$$v_a \equiv \overline{v^2}^{1/2} = 2.3 \times 10^7 \text{ m/s} \quad (12)$$

and

$$\mathcal{E}_a = \frac{m}{2} \overline{v^2} = 2.4 \times 10^{-16} \text{ J} \quad (13)$$

or

$$\mathcal{E}_a = 1.5 \text{ keV} .$$

While the free-field distance of travel of electrons would be  $2x_a$ , when we consider that their position at the start of a bombarding cycle would be random with respect to the surface, then we should average over the phase of the harmonic oscillation, which introduces a factor  $2^{-1/2}$  and reduces the average thickness of the bombarding sheath to

$$x = \frac{2}{\sqrt{2}} x_a \approx 0.5 \text{ mm} .$$

Note that this use of average energy really is conservative. The peak electron energy, on the equator, is

$$\mathcal{E} \approx 9 \text{ keV.}$$

Incidentally, since  $v/c \ll 1$  the magnetic forces were ignorable as assumed.

Now, with these keV electrons bombarding the surface and incident normally, secondary emission is at its maximum (Refs. 14 and 15). A reasonable value for the excess in secondary emission is  $S = 0.5$  (where  $1 + S$  is the usual secondary emission coefficient). The exact value of  $S$  does not matter since the electron density grows at a rate  $\exp(Sft)$ , because the electrons hit every other half cycle of the frequency  $f$  and grow to a density

$$n \approx 10^{14} \text{ cm}^{-3}$$

in 6 ns if  $S = 0.5$  and in 64 ns if  $S = 0.05$ . The electron growth is fast compared to the pulse length and to all the other effects analogous to other electron avalanche processes such as breakdown and multipactoring.

The growing electron plasma is also trapped by the ponderomotive well (discussed in last year's report, Ref. 16) which is produced by the interference of the incident and reflected wave, and by the electrostatic forces of the surface (positive) and space charge (negative) trapped in the well. As long as the plasma is mostly electrons there are no loss mechanisms, except to bombard the surface and produce more electrons (radiation loss is small since  $v/c \ll 1$ ), so the electron plasma grows quickly.

The question then is to determine how large the electron density would have to be before all of the incident power is transferred into simple harmonic motion of the electrons, which lose energy to the surface. That would limit the growth of the electron plasma. The electrons in the bombarding sheath,  $x_s$ , hit the surface every other half cycle with frequency  $f$ , so the average power per unit area transferred to the surface is

$$\frac{dP}{dA} = n e_a x_s f \quad , \quad (14)$$

and for the values cited above,

$$n \approx 2.5 \times 10^{14} \text{ cm}^{-3} \quad ,$$

which is reasonable. Presumably, in the early stages, when the plasma layer is thin, it might grow to that density since the electrons are so energetic (1 keV). However the critical density for  $f = 10$  GHz is  $n_c \approx 10^{12} \text{ cm}^{-3}$ .

After some ions have been added to the electron plasma, the plasma will be shielded to the collisionless skin depth, about 0.5 cm, close to the thickness (about one quarter wavelength) of the plasma layer trapped in the ponderomotive well, so a decrease toward critical density would be expected and the energy transferred to the surface would be of order one tenth of the incident energy because of microwave reflection from the plasma.

When the plasma has become fully neutralized by ions from the surface, other phenomena than the electron plasma could dominate. The role of ions, longitudinal plasma waves (Langmuir oscillations), and plasma shock waves will be examined next year, but the important point is that the normal electric fields which we are studying are much larger than anyone has tried to use in plasma etching and sputtering before. It would be surprising if

the ablation rate of the surface would not be predicted to be large indeed. Arcing and its relation to balloon-popping also needs to be checked.

The important implication of our simple model is that the power density deposited in the thick metal film is proportional to  $E_n^3$ . This should cause a field and geometrical dependence of electron plasma demetallization, which can be checked experimentally; so far all our experiments have been performed for near-normal incidence, in order to test the theory of direct heating.

### 3.2 TASKS 4 - 6: EXPERIMENTAL STUDY OF HPM/TARGET INTERACTIONS

Our program of experimental measurements addresses the in-vacuo physical-damage mechanisms and decoy signature modifications possible through HPM irradiation. The first objective is to establish, within a high-vacuum target chamber with dielectric input and exit windows, the basic vulnerability levels of simple decoy systems such as plastic substrates metallized to different layer thicknesses, radar chaff, optical corner reflectors, and heat shield materials.

To evaluate the energy-deposition requirements for ablating aluminum from decoys, we performed simple ablation experiments on a hypothetical decoy material. We exposed aluminized Kapton to high-power microwave pulses in evacuated C-band waveguide. By testing different thicknesses of aluminization, we were able to compare our experimental results with the predictions of our analytical model (cf. Section 3.1). The test results, which ranged from almost complete ablation of thin aluminum coatings to minor damage on thick ones, are in reasonable agreement with the analytical model.

#### 3.2.1 Experimental Apparatus

Figure 6 illustrates the experimental configuration schematically. We mounted target foils consisting of 12.5- $\mu\text{m}$  thick Kapton (polyimide) sheet coated with various thicknesses of

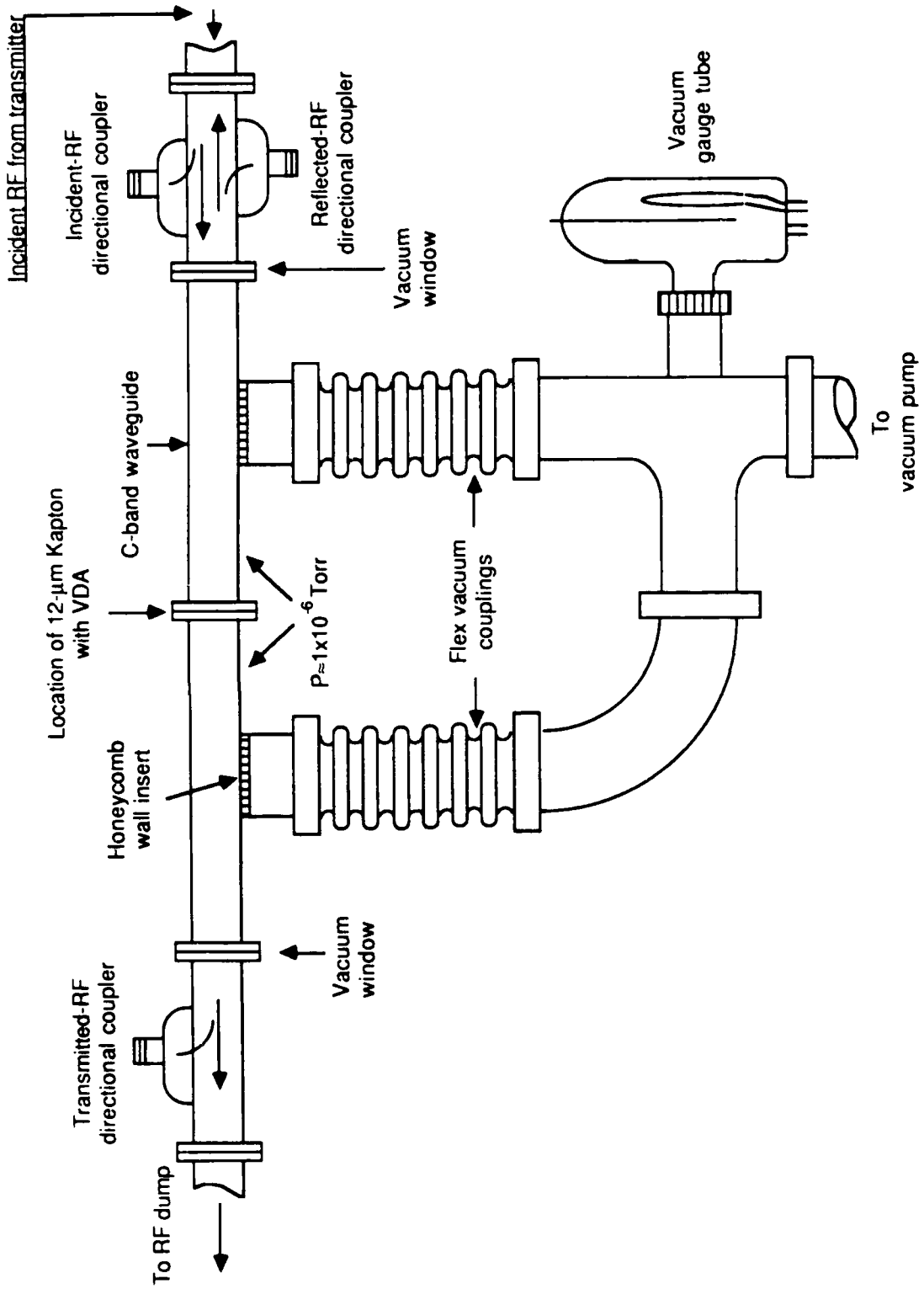


Figure 6. Experimental apparatus.

vapor-deposited aluminum (VDA) directly inside an evacuated section of C-band waveguide. The waveguide is evacuated on both sides of the target foil by a small turbomolecular pump; sections of metal honeycomb are brazed into the waveguide walls to afford good vacuum pumping speed with minimal perturbation to microwave propagation in the guide. This system produced prepulse pressures below  $10^{-4}$  Pa ( $10^{-6}$  Torr). Directional couplers on both sides of the target foil permit measurement of incident, transmitted, and reflected microwave power levels.

Microwave power is provided by a C-band transmitter consisting of a traveling-wave tube (TWT) and cross-field amplifier. The output consists of 40- $\mu$ s-long pulses at a peak power of 580 kW, providing a maximum energy deposition of 22 kJ/m<sup>2</sup> (2.2 J/cm<sup>2</sup>). In our experiments, we used a burst of three pulses, spaced 40 apart, because the transmitter could not achieve maximum output power in a smaller number of pulses. Calculations show that energy deposition from the first two pulses, which are at reduced power, should have little effect on the experimental outcome, because the long interpulse period is sufficient for the foil to radiatively cool to a temperature close to ambient.

### 3.2.2 Test Results

As expected, the extent of damage varied strongly with VDA thickness. The 10-nm-thick VDA was almost totally vaporized. The samples having 20-nm and 50-nm-thick VDA were significantly damaged, but only minor striations of ablation were noted on the 70-nm-thick VDA. Figures 7, 8, 9, and 10 show enlarged photos of four foils, giving the associated incident power levels. The actual size of the damage area corresponds to the inside dimensions of the C-band waveguide, 47.5x22.1 mm (1.87x0.87 in.). The mottling and striations in the remaining VDA are striking features in these photos; material inhomogeneities of the Kapton and/or the VDA may precipitate this effect. (Regions of thin VDA would ablate faster, leading to lower conductivity, higher electric fields, and even larger ablation rates).

M17749-16

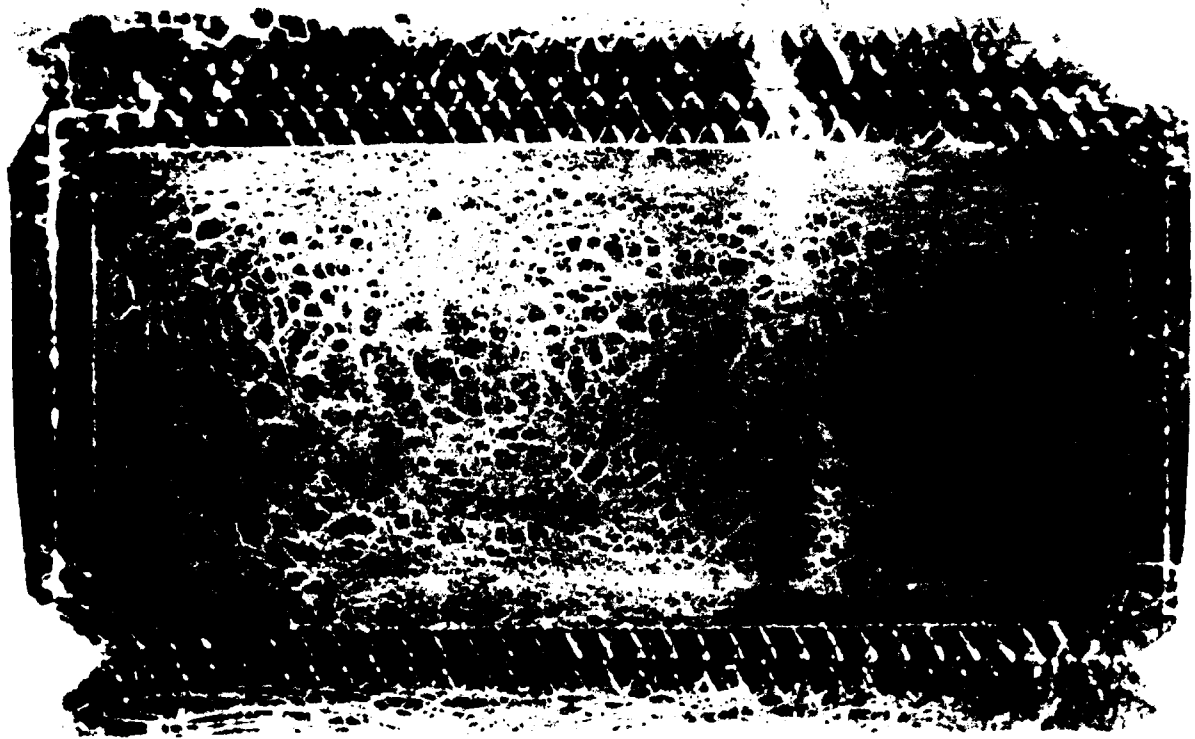


Figure 7. Photograph of 12.5- $\mu\text{m}$ -thick Kapton sample with 10-nm-thick VDA coating, following 45-kW/cm<sup>2</sup>, 40- $\mu\text{s}$  HPM exposure.

M17750-8

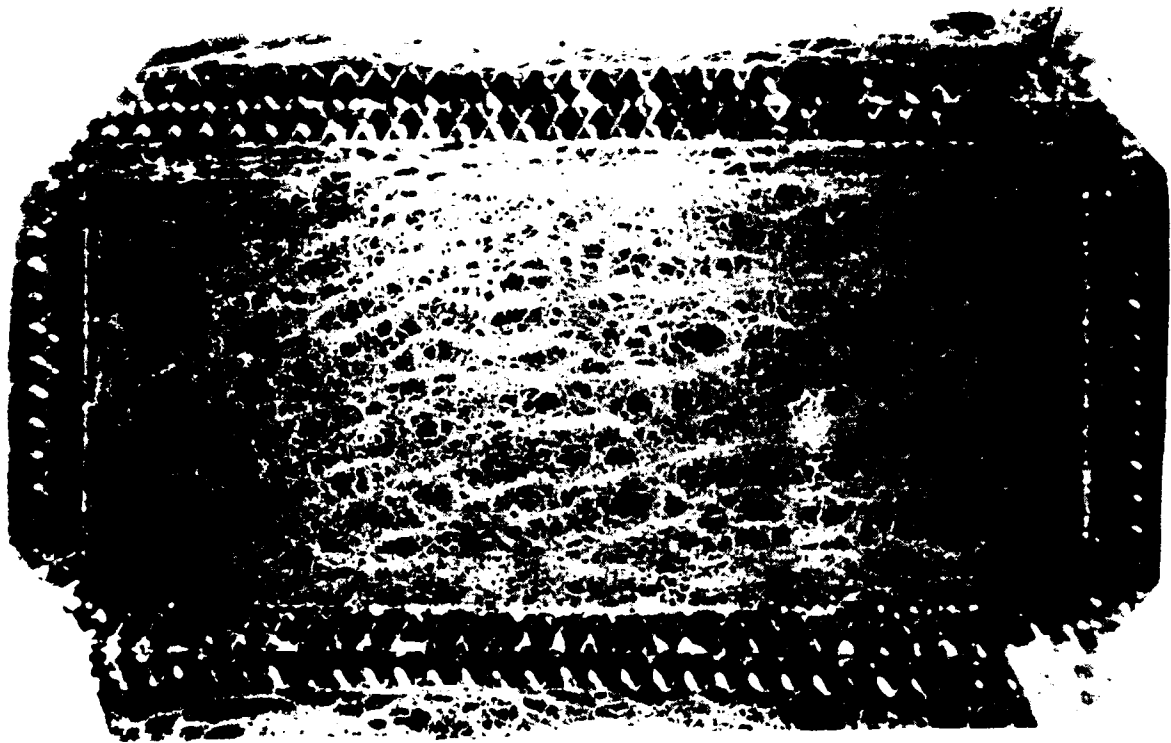


Figure 8. Photograph of 12.5- $\mu\text{m}$ -thick Kapton sample with 10-nm-thick VDA coating, following 44-kW/cm<sup>2</sup>, 40- $\mu\text{s}$  HPM exposure.

M17752-2

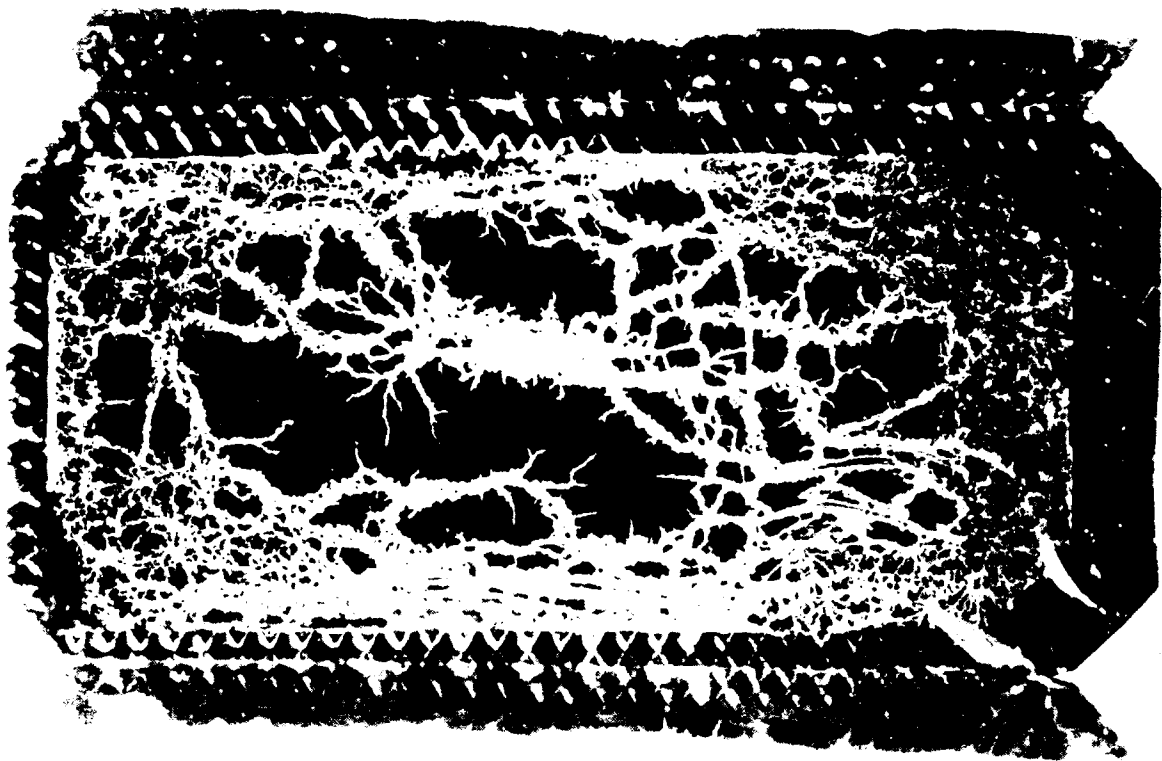


Figure 9. Photograph of 12.5- $\mu\text{m}$ -thick Kapton sample with 20-nm-thick VDA coating, following 68-kW/cm<sup>2</sup>, 40- $\mu\text{s}$  HPM exposure.

M17751-10

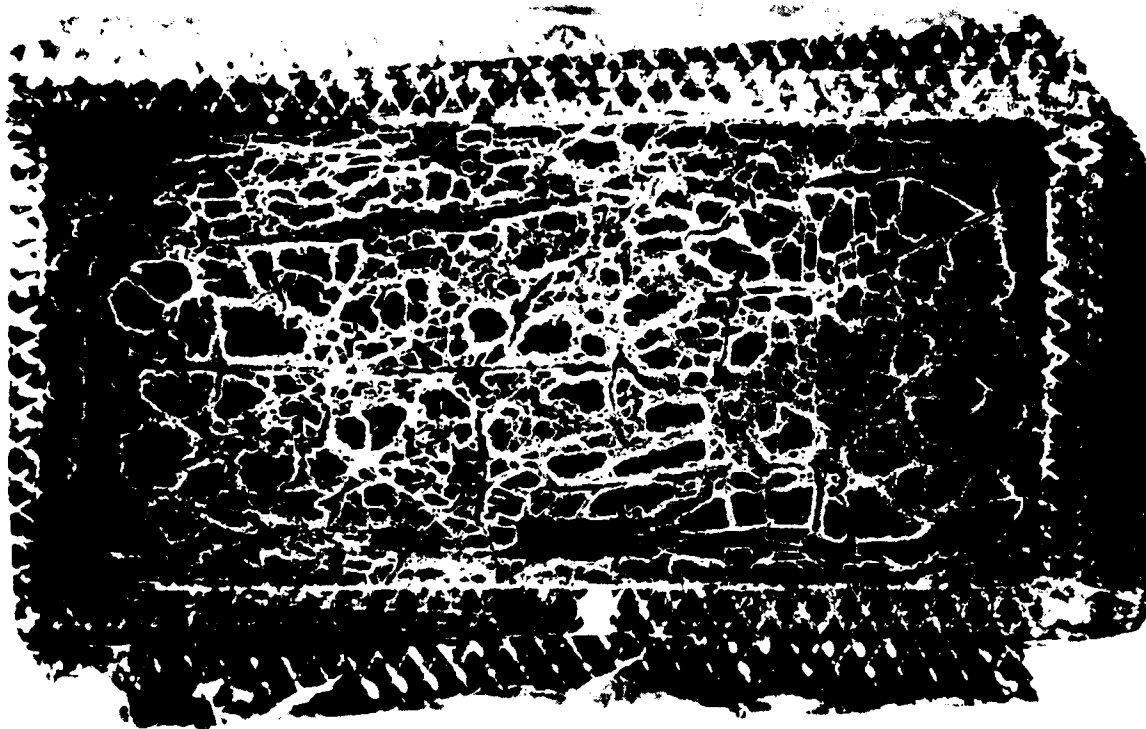


Figure 10. Photograph of 12.5- $\mu\text{m}$ -thick Kapton sample with 50-nm-thick VDA coating, following 42-kW/cm<sup>2</sup>, 40- $\mu\text{s}$  HPM exposure.

### 3.2.3 Comparison with Analytical Model

The experimental results agreed with the predictions of our analytical model. The onset of observable VDA ablation occurred at approximately the power level calculated by the model. The amount of ablation as a function of VDA thickness (at a given power density) is also in qualitative agreement with the theoretical predictions. Table 3 shows a comparison between the predictions of the analytical model (cf. Section 3.1 ) and our experimental results.

While good qualitative agreement clearly exists, the quantitative comparison of the four experimental results with model predictions is affected by two factors. First, we discovered that the leading edge of the RF power pulse contained a very brief precursor spike that was significantly higher in power than the remainder of the 40- $\mu$ s pulse. Second, we often experience high-voltage breakdown in the waveguide (predominantly at the vacuum windows), making it difficult to perform an unambiguous single-shot experiment. Arcing may also have occurred on the target surface (an alternative possible explanation for the striations). Neither of these effects is represented in our analytical model.

A number of revisions to the experimental apparatus are planned to circumvent the arc-breakdown problems which prevented investigations at higher incident energy densities. Brief descriptions of the difficulties and of our planned revisions are given below.

### 3.2.4 Limitations of Present Apparatus

The combination of HPM and high vacuum resulted in electrical breakdown in the evacuated waveguide section between the vacuum window and the target foil. Once an arc had occurred at the vacuum window, the window would continue to break down even at lower power levels. In addition, breakdown at the window

**TABLE 3. Comparison of Exerimental Results and Analytical Model Predictions**

Polyimide Substrate Thickness: 12.5  $\mu\text{m}$

Pulse Length: 40 $\mu\text{s}$

Power Density: 42 to 68  $\text{kW}/\text{cm}^2$

Original VDA Thickness	Predicted VDA Loss, as Percent of Original Thickness	Observed Result	Corresponding Figure No.
10 nm	100%	Almost Complete Removal	7, 8
20 nm	100%	Major Damage	9
50 nm	10%	Significant Damage	10
70 nm	0%	Minor Damage	--

could not be distinguished from breakdown at the foil sample. Arcing was more likely to occur when a foil was in place since the reflected energy produced a standing wave with the incident energy and increased the electric field at particular locations. The window was designed to be at a node of this standing wave, but when a breakdown occurred at one of the peaks, the window could be located at a peak of the new standing wave reflected from the position of the breakdown. The honeycomb pumping ports were necessarily large to provide adequate pumping speed. This caused part of the port to be in the high-field region of the waveguide; the edges of the honeycomb therefore provided initiation points for breakdown.

### 3.2.5 Planned Apparatus Revisions

We plan to design and construct a revised vacuum waveguide section to produce more than four times the mean incident power density that we are presently using, and we also plan to incorporate a new TWT into the C-band system, which should give us a peak-power capability of 800 kW. These revisions will permit us to operate at much high power densities and to make more quantitative comparisons with our model.

Figure 11 shows the planned system revision. The waveguide will be tapered up in height to reduce the microwave power density on the vacuum windows. The waveguide will then be tapered down to 1/4 the normal C-band vertical dimension (the guide width, which determines the cutoff frequency, will remain the same). Also, the pumping ports will be placed on the sides of the waveguide where the electric fields go to zero (there will be sufficient grid structure to allow wall currents to flow with minor perturbation). These modifications will increase the incident power density at the foil surface by a factor of four. With the added power of the new TWT, the projected increase in power density is almost six times that of our latest tests.

17808-37

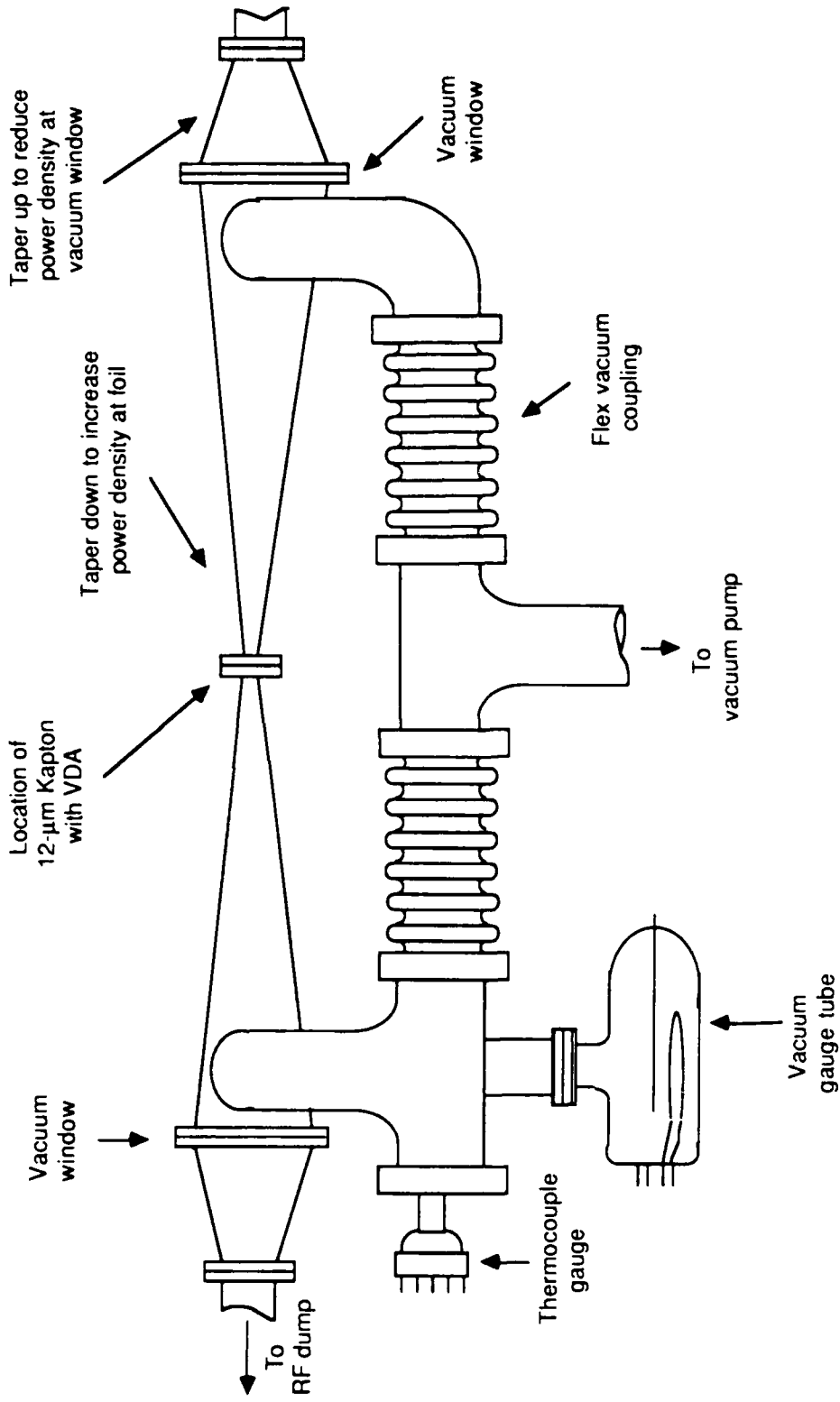


Figure 11. Revised system.

In our future experiments we will employ improved instrumentation and noise-suppression methods. This will allow us to accurately evaluate the time dependence of the incident power so that a more representative pulse shape can be used in the analytical modeling. This approach will accommodate effects produced by the presence of a precursor spike or other pulse shape characteristics.

### **3.3 TASK 7: SURVEY OF THE STATE OF THE ART IN HPM TECHNOLOGY**

This section presents a brief historical overview of high-power microwave sources, establishes those characteristics which define the state of the art as of October 1987, and outlines some of the advances, most unpublished, in the technology of source development up until December 1987.

There has been a dramatic increase during the past ten years in the basic and applied research devoted to high-power microwave source development. Prior to this period, research performed on high-power microwave (GW level) sources was not so intense, at least in the United States. This was due in part to the arrival of sophisticated phased-array radar systems enabling higher powers on target without necessarily requiring higher power sources; this, when coupled with advanced radar signal processing techniques, removed the sense of urgency from high-power source development.

With the arrival of large pulse-power assemblies, and especially with advances in electron and light-ion accelerator technology, both for fusion and directed-energy weapon (DEW) purposes, the stage was set for substantial advances in microwave source development. Without the great cost savings afforded by these existing systems (including nuclear weapons effects simulators such as Aurora and Shiva-Nova), HPM source development would not be as advanced as it is, since the utility of microwave damage as a kill technique has not been demonstrated to everyone's satisfaction, and until recently this was a major

obstacle to funding. As it happens, a major portion of present-day funding is devoted to vulnerability testing; innovative program managers have always been able to tax their testing programs to produce more "appropriate" microwave sources.

A second reason for increased HPM funding has been the knowledge that the Soviets were very active in this research area, with rather remarkable claims in the open literature concerning high powers and efficiencies in microwave power generation. Some of the earliest Air Force Weapons Laboratory funds were spent in applying sophisticated computer codes to verify these claims.

Despite the recent advances in source development, the "perfect" HPM generator does not exist, whether for a weapon or for a test device. This is due to the large matrix of desirable generator characteristics (not to mention the inability of present compact power supplies to run these devices). These desirable features include high power (GW or more), long ( $\mu$ s, variable) and short pulsewidths, high pulse repetition rates, frequency tuning (0.5 to 50 GHz, for example), short risetime ( $< 1$  ns), no prepulse, shot-to-shot reproducibility, high efficiency ( $> 20\%$  plug to RF, especially important for a DEW), ease of maintenance, long lifetime, small size, etc. Some of these features are more desirable for testing purposes than for a DEW system.

Among the devices which have received a large share of experimental research attention have been the virtual-cathode machines, back-wave oscillators, free-electron lasers, cyclotron masers, and cross-field oscillators/amplifiers.

### 3.3.1 Virtual-Cathode (VC) Devices

This class includes the virtual-cathode oscillator (VCO, or Vircator) and the reflex-electrode type devices.<sup>17</sup> The device works by allowing an intense relativistic electron beam to propagate into a drift tube, where if the space-charge limited

current is exceeded, a space charge is generated leading to the production of a virtual cathode. This plasma cathode oscillates axially and radially. In addition, electrons that are caught between the real and virtual cathode are forced back and forth, i.e., are "reflexed." In some machine configurations oscillating virtual cathodes are the predominant microwave radiation mechanisms, while in others, the reflexing electrons are the cause.

Virtual-cathode devices are easy to manufacture, are simple and robust, and easily tunable, are amenable to computer modeling and attach easily to a wide variety of relativistic electron beam (REB) devices. Moreover, they can be run in a rep-rated mode, with the choice of a wire-mesh anode or a "foil-less" anode using external magnetic fields and the drift tube walls as the anode. On the negative side, there is intense mode competition within the cavity, there occurs frequency chirping during a single shot, and pulsewidths tend to be short due to anode-cathode gap closure. Still, the records for achieving the highest peak power belong to this class of machine (44 GW, pending proper diagnostic analysis, HDL). As spectacular as this may be, perhaps more intriguing are the complementary efforts underway in a number of laboratories, aimed at removing the undesirable features of VC devices. The favored approach is the use of a cavity tuned to a resonant mode. This will allow easier extraction of power, perhaps by several slots in the cavity, permitting low power densities at each output. As important as locking in the proper mode may be for transmission and antenna considerations, the added benefit of possibly achieving narrow bandwidth may ultimately permit cavity pumping using a number of sources, thereby allowing appreciable increases in efficiency. The problem associated with narrow pulsewidth is also being attacked by careful attention to diode design, both with respect to geometry and materials science.

### 3.3.2 Free-Electron Lasers (FELs) and Cyclotron Masers (CMs)

At the other extreme to the fire-breathing virtual cathode machines are the laser/maser and related devices, which have as their major characteristics superior phase and frequency coherence. Although conceived as devices to operate at IR and optical wavelengths, FELs work well at millimeter wavelengths, and there is no reason why they should not perform at centimeter ones. Due to the small bandwidths achievable with FELs (and maser devices), a favored approach is to use many relatively low power output devices ganged for efficiency; by adding modules it is hoped that GW outputs can be achieved. This approach is being followed by NRL.<sup>18</sup> Since high current densities are not necessary for FEL operation, there need be no diode closure problems, allowing long-pulse operation, although this has not been demonstrated for high powers. Although "tunability" is usually achieved by changing magnet dimensions, periodic plasmas are being examined for possible use. Cyclotron masers work by the gyrations of injected REB around magnetic field lines at the cyclotron frequency which depends directly on the magnetic field strength and varies inversely with electron energy. Coherence is achieved by orbital phase bunching. The best-known examples are the gyrotron and the cyclotron auto-resonant maser (CARM). The major difference is that CARMs convert longitudinal rather than transverse electron kinetic energy to RF radiation. CM devices are tunable via adjustments to the externally imposed axial magnetic field and the electron beam voltage; however, efficient operation requires REBs with low energy spread. The CARM operating frequency increases with beam voltage, but Gyrotron frequencies decrease with higher voltage. For this reason, CARMs can operate at frequencies higher than 100 GHz. Gyrotrons have operated at GW levels, at pulselengths of tens of nanoseconds. This pulselength may be lengthened appreciably (with reduction in power) by the use of thermionic rather than field-emitting cathodes. CMs should be capable of appreciably high repetition rates.

### 3.3.3 Back-Wave Oscillators (BWOs)

Back-wave oscillators produce RF via the interaction of REBs with a slow-wave structure. Microwaves are generated by plasma instabilities that grow as the group velocity proceeds counter (backward) to the electron beam direction.

BWOs have been favored (since their inception by Rukhadze in 1976) for their promise of high power levels ( $> 20$  GW), amenability to high pulse repetition rates, microsecond pulsewidths, high efficiencies ( $> 20\%$  e-beam power to RF power) and wide range of frequencies (although after beam and cavity parameters are set, only minimal tuning is possible). As yet, the promise of smooth operation at power levels above about one GW has not been realized. If the 10-GW barrier is successfully exceeded, there is no guarantee that pulsewidths will be satisfactorily long, although the handicaps of short pulsewidths may be partially offset by high pulse repetition rates (which may, however, stretch capabilities in the pulsed power community). As with all devices that are "well understood" at low output levels, the leap to higher output levels raises the importance of issues which were only of second-order importance at low levels: better understanding of plasma instabilities, self-induced magnetic effects, space-charge considerations, production of ion currents, etc.

### 3.3.4 Cross-Field Oscillators/Amplifiers (CFOs/CFAs)

Although cross-field devices such as magnetrons and klystrons have been in operation for decades, new wrinkles in design point toward high power levels at very narrow bandwidths. Of particular interest is the magnetically insulated transmission line approach. In concept, the device is a front-wave oscillator wherein, like in a BWO, a corrugated or periodic anode interacts with an REB, and the difference between phase and group velocities in the forward direction causes the plasma

periodicities which cause RF emission (a common "front-wave oscillator" is the traveling wave tube, TWT). Unlike conventional magnetrons and klystrons, the magnetically insulated transmission line devices require no externally imposed magnetic field, inasmuch as the magnetic fields are self-generated. This leads to extremely high (100s of kiloamperes) current handling capability; moreover, since the self-magnetic field and acceleration voltage are produced from the same electrodes, high voltages can be used without breakdown, due to small potential differences. Interaction volumes can therefore be large, avoiding breakdown and space-charge effects (at the price, perhaps, of competing modes). Since the magnetic field is self-generated, variations in line voltage are self-compensated. Of particular interest is the "system-friendly" nature of the device; pulse-power/power-conditioning requirements are not demanding, repetitive operation is possible, energy extraction and antenna transmission appear not to be severe problems, and operation in amplifier modes appears straightforward. It remains to be seen if experiments will match the computation predictions.

Developments with other CFO/A devices have also been substantial. It is pointed out that the HPM device with highest output power reported in the Soviet literature is a magnetron (8.5 GW, 2.4 GHz, 40 ns width). Developments in this country using externally imposed axial and radial fields are producing GW power levels. The Bekefi "A6" magnetron uses a radial electric field with an axial magnetic field. The magnetron "cavities" are formed by ripples in the cavity wall.

Recent research with relativistic klystrons is also producing improvements in high-power operation. One variation, the Varian Lasertron, uses laser-induced (monochromatic) photoelectron bunches.<sup>19</sup> In addition to avoiding the electron energy spread seen in conventional klystrons, high power densities, even in small interaction volumes, may be possible (an added benefit is the absence of competing modes).

### 3.3.5 Cavity Compression

One of the few classes of device not driven by REBs are the time and field compression cavity devices. Basically, the idea with time compression is to fill an RF cavity via an RF pump (e.g., klystron). If the cavity can be emptied rapidly (when compared to filling times), substantial power gains may be realized. RF field compression involves the rapid mechanical squeezing of cavity dimensions. Both techniques have not yet produced significant power outputs. We mention them because of the possible role that high-temperature superconducting materials may play in power amplification.

### 3.3.6 Summary

Two approaches to HPM (10s of gigawatts) generation are underway. One approach is to use existing high-power sources of "poor" quality (high bandwidth, variable voltage, poor electron beam emittance, etc.) and try to produce mode locking and power injection. A good example is the use of virtual-cathode devices in conjunction with resonant cavities. The other approach is to use modules of devices with high-quality RF characteristics which lend themselves to oscillator-amplifier operation. A good example is the use of low-power (few megawatts), long-pulse (thermionic) gyrotrons, suitably coupled. Of course, the best of both worlds would involve gigawatt outputs of high-quality modules. One standout in this area appears to be the Lawrence Livermore ETA-driven FEL (1.8 GW, 34.6 GHz, e-beam/RF efficiency of 42%, and a pulse repetition rate of 0.5 Hz). Major drawbacks include the need for good electron beam quality, complexity, lack of tunability, and short pulsewidth due to gap closure induced by diode geometry.<sup>20</sup> Soviet gyrotrons have also been run at the same power level (2 GW, 3.1 GHz, 40 ns width). Gyrotrons have the added feature of tunability (not as impressive as the virtual-cathode machines, however). One must say that barring

breakthroughs in research concerning other devices, gyrotrons are extremely promising for extremely high power. An overview of U.S. and U.S.S.R. HPM experimental results is given in Tables 4 and 5, respectively.

### **3.4 TASKS 8 - 10: SYSTEM DESIGN STUDY**

The conceptual design of an overall decoy discrimination system is an important step in the process of demonstrating the practicality of the proposed concept. The following issues must be addressed in the course of a study leading to an overall system design: trade-offs between range and hardware requirements, number of systems required, pointing and tracking requirements, time required to discriminate, low/high power operation for look-shoot-look capability, HPM source module rating optimization, trade-offs between amplifiers and phase-locked oscillators, large-aperture phase sensing and control, dimensional stabilization of large antenna arrays, trade-offs between microwave and optical carriers for distribution of the excitation signal, prime power source selection, optimization of power conditioning method, and conceptual hardware installation layout. The objective is to develop one (or several alternative) conceptual system design(s) on the basis of the results of this study.

The system design study effort this year was concentrated on the establishment of bounds on some important parameters of the phased-array antenna system.

#### **3.4.1 Phased-Array Beam Steering and Focusing**

With a sufficiently dense array of phase shifters, it is possible to phase steer a transmitted beam to any angle within the field of view of the array. The following discussion describes how densely the phase shifters must be placed for various beam steering fields of view. Since very large arrays will require huge numbers of phase shifters, the total system cost may be strongly affected by the phase shifter density and unit cost per phase shifter.

TABLE 4. U.S. HPM Experiments.

OSCILLATOR TYPE	POWER (MW)	VOLTAGE (MV)	FREQUENCY (GHz)	EFFICENCY (%)	PULSEWIDTH (ns)	LOCATION
Viracator	350	1	1-11		65	PI
Viracator	2000	8-12	1	1.4	132	LANL
Viracator	15-350	1	1	0.04-1		MRC
Turbutron	44-200	8	1	1-2	150	ND, SNLA
Magnetron	1500	1	2.8		65	PI
Gyrotron	0.645	0.08	140	24	3000	MIT
Gyrotron	0.2	0.08	140	30	1 ms	Varian
Gyrotron	0.6	0.1	35	50	10-50 $\mu$ s	Varian(NO*)
Gyrotron	100	0.6	28-49	8	20	NRL
Lg. Orbit Gyrotron	500	23	12-18	10	5-15	U of M
CFO		0.4	0.72, 1.4		50	SNLA
CFO	50	0.15-0.58	3.6	1	80	AFWL
Lasertron	1500	0.6-1	2.8	67	1000	Varian(NO)
CARM	30	0.5	44	30	10-20 $\mu$ s	Varian(NO)
BWO	16	0.6-0.7	8.8	1	70	HDL, SNLA
FEL(amp)	1800	3.6	34.6	45	20-25	LLNL
Beam Plasma Device	18000	1.4	2-6		60	LLNL
Scantron	1000	1	1	30	1000	Pulse Sci. (NO)
Klystron						LLNL Stanford Berkely

\* Not Operational

TABLE 5. U.S.S.R. HPM Experiments.

OSCILLATOR TYPE	POWER (MW)	VOLTAGE (MV)	FREQUENCY (GHz)	EFFICIENCY (%)	PULSEWIDTH (ns)
BWO	1000	0.670	9.4	30	15
BWO	5000		9.5	10	30-50
Magnetron	4000		9.1	15	20
Magnetron	8250		2.4	47	
Gyrotron	2000		3.1	30	40
Gyrotron	20-30		79-107		
Vircator	1400	0.450	3.3	12	40
Vircator	120		3.3	37	1300
CARM	580	0.650	10	15	55
Orotron	1400	1.3	7.5	10	
FEL	300		17		10
Plasma Cherenkov Maser	100	0.480	10	21	50
Microwave Resonator	70		3		15

Anticipating the final result, it is shown that beam steering over approximately a 60° field of view requires that phase shifters be spaced at one wavelength intervals. Larger steering angles require smaller phase shifter spacings, perhaps as small as half wavelength spacings. In general, each phase shifter must have a different phase setting than its nearest neighbor. It is shown to be not practical to steer a transmitted beam by using patches of phase shifters with identical phase settings; i.e., the size of the largest practical patch is on the order of one square wavelength.

Beam focus is also related to beam steering. It is necessary not only to point the beam in the desired direction but also to bring it to a focus at the desired range. While beam steering requires linear phase tilts across the array, beam focus requires an additional quadratic phase correction across the array to launch converging spherical waves. The quadratic phase corrections must be algebraically added to the tilt signals at each phase shifter. Again anticipating the result derived below, beam-focus phase corrections can be done in patches as large as 250 m.

The implications of these results for the decoy discrimination system are very important. At an operating wavelength of 3 cm and an array diameter of 10,000 m, the array is 333,333 wavelengths in diameter and contains  $8.7 \times 10^{10}$  square wavelengths of area. To be practical, phase-shifter costs must not totally dominate the system budget. A reasonable goal might be for phase-shifter costs no more than about \$0.10 per shifter. The cost must include the method for addressing and setting the required phase shifts, such as a wire connection to each shifter. Although such costs are far below currently available phase-shifter components, they may be achievable with innovative designs such as printed circuit arrays which are discussed elsewhere in this report.

### Far-Field Radiation Patterns from Phase-Steered Antennas.

Consider a phase-steered antenna consisting of a closely packed two-dimensional array of sources. Each source is a small square approximately one wavelength on a side. Each source radiates single-frequency waves from its upper surface with an adjustable phase relative to its neighbor. A cross section of the antenna is illustrated in Figure 12 as a line of sources.

Now consider the radiation pattern from just one of the sources. For rectangular sources, the far-field pattern may be calculated in closed form and is found in most text books on diffraction theory. It has the form of  $\sin(\pi L/\lambda)/(\pi L/\lambda)$ , where  $L$  is the length of the source and  $\lambda$  is the wavelength. The far-field intensity pattern is the square of this function. A computer calculation of the far-field intensity pattern is illustrated in Figure 12 for a source size  $L$  equal to the wavelength of 3 cm and a target range of  $3 \times 10^6$  m. The cross range is given in units of  $10^6$  m.

Because of diffraction, a single small source spreads its illuminating power over a large area. Several general features are immediately apparent. For the one-wavelength-long source shown here, the half-power points in the beam are approximately  $60^\circ$  apart; i.e., the cross-range width is equal to the down-range distance. The smaller the source length  $L$ , the wider the far-field pattern. Each individual source in the array has this same relatively wide far-field pattern, and all sources in the array illuminate the same field of view.

Very narrow beams within the field of view may be formed by coherently interfering the contributions from many small sources. Figure 13 shows the far-field beam patterns for closely packed arrays of lengths 10 and 100 wavelengths, respectively. The beam patterns are exactly 10 and 100 times narrower than the beam for a single element of the array. For comparison purposes, the peak on-axis intensities have been normalized to the same scale factor.

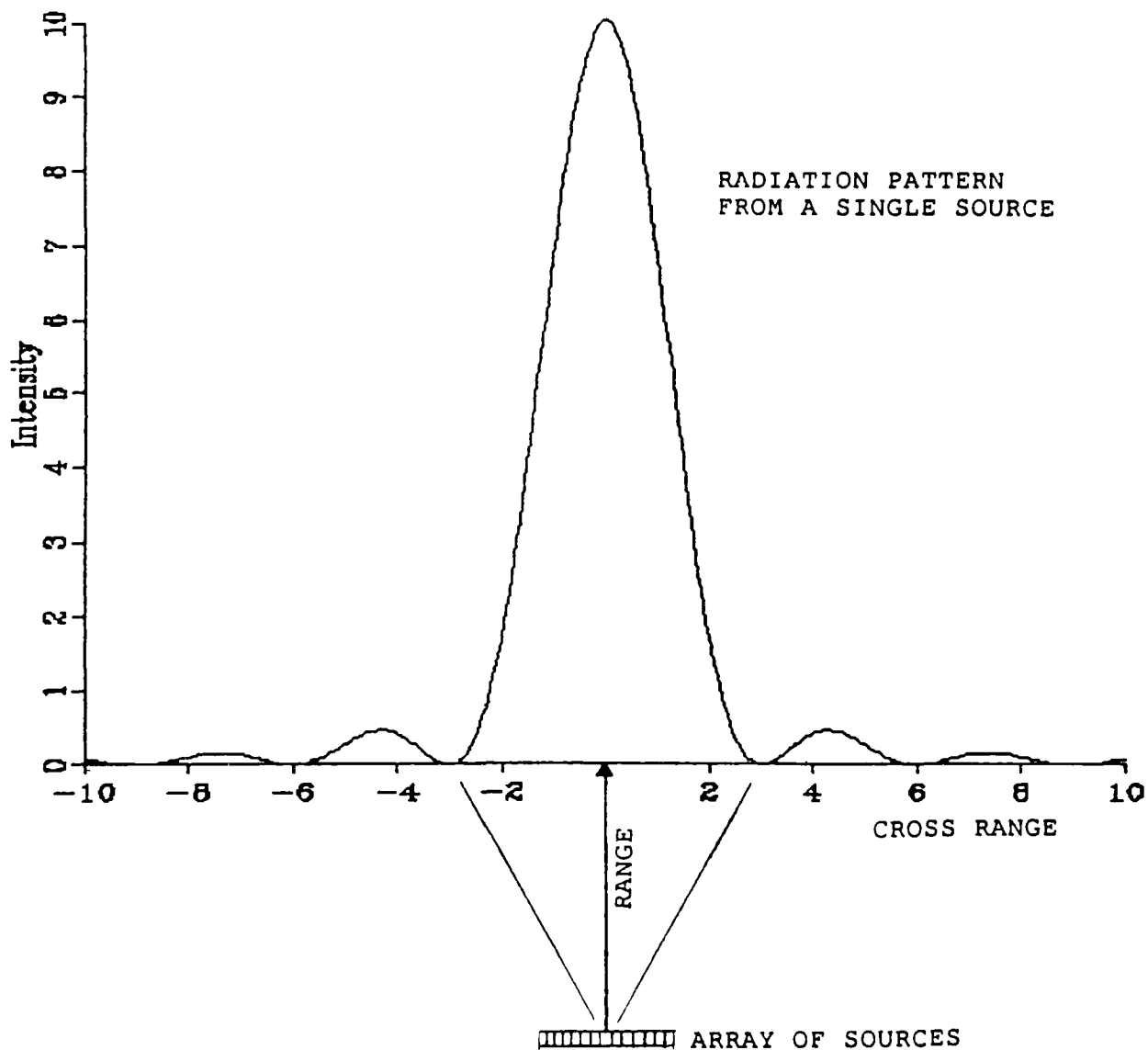


Figure 12. A single array element has a wide field of illumination. Here, each element is one wavelength square and illuminates a cross-range distance approximately equal to the down-range distance.

17808-2

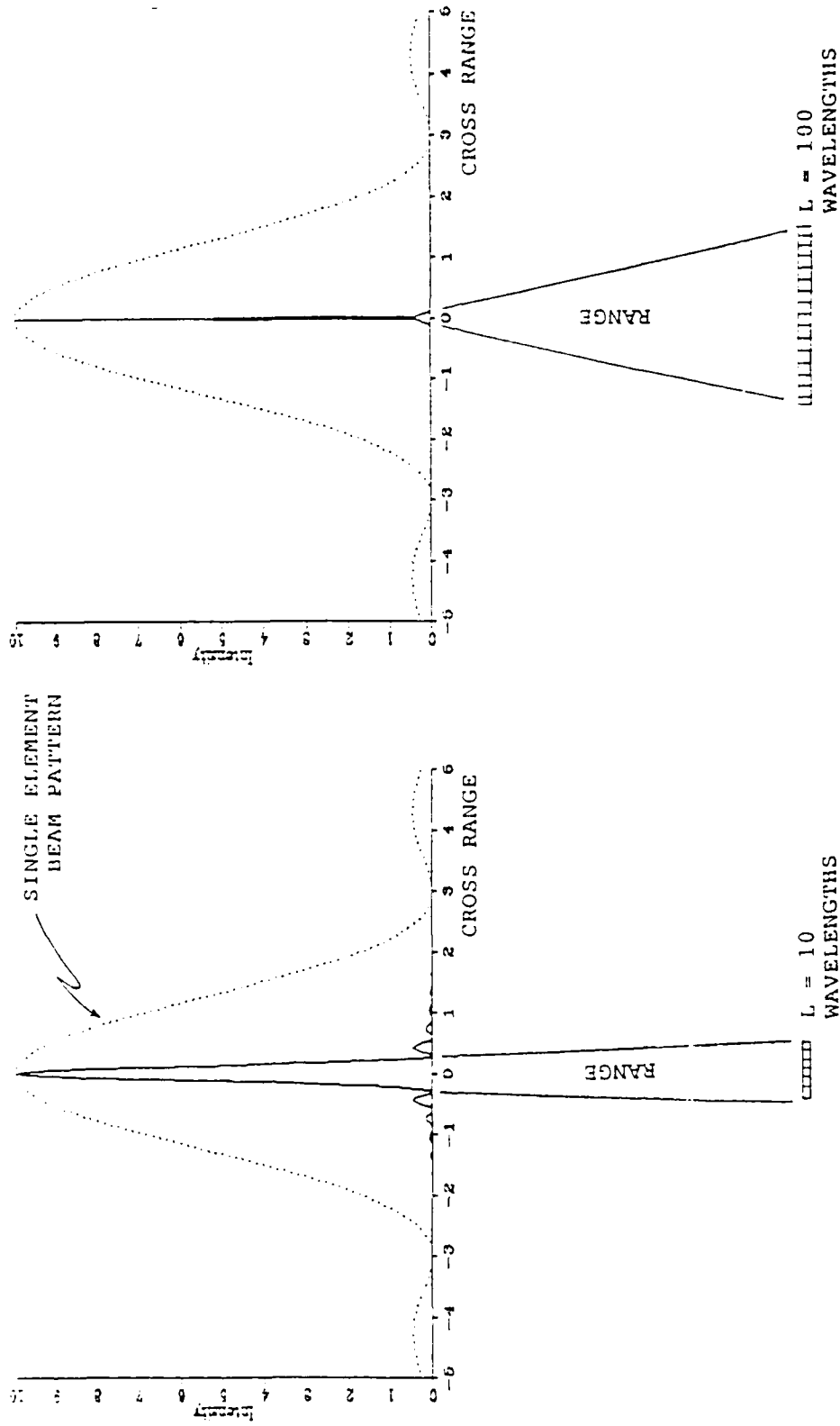


Figure 13. Extended arrays can form narrow beams when the contributions from each element arrive in phase at a distant point.

An interesting phenomenon may be seen when the beam is steered to an off-axis direction. Figures 14(a-e) show the far-field pattern as the beam is progressively steered to the right. Beam steering is accomplished by introducing progressive phase shifts from element to element across the array.

As the beam is steered to the right, the maximum beam intensity drops and two side lobes appear. The total power in the beam is shared between the main lobe and the side lobes. The main-lobe peak intensity closely follows the outline of the beam pattern from a single element. The side lobes follow somewhat different curves. The three lobes may be thought of as diffraction grating orders. The main lobe is the zeroth order. The lobe to the right is the +1 order and the lobe to the left the -1 order. The three lobes steer at different rates. For example, Figure 14(c) shows the main lobe steered one division to the right. The -1 order has moved 1/2 division to the right and the +1 order has moved 1 1/2 divisions.

Since the main-lobe power falls off with large steering angles, in radar systems there is usually not much point in steering beyond the half-power points or about 1 1/2 divisions on the scale shown here. For a discrimination system, however, the performance criteria may be considerably different than for a conventional radar. Half of the power in the beam may be very adequate to discriminate some targets at the nearer ranges. By tolerating very high side-lobe levels, a discrimination system can achieve beam steering over wide angles with about a factor of four fewer phase shifters in the transmitting antenna than a search radar.

The envelope of the power curve is determined by the size of the individual element in the array. Since the cases shown here are for one-wavelength-long elements, the half-power steering angle corresponds to approximately a 60° field of view. If the element size is reduced to 1/2 wavelength, the half-power field of view will be extended to nearly 120°, but the cost then increases from one to four phase shifters per square wavelength in the antenna.

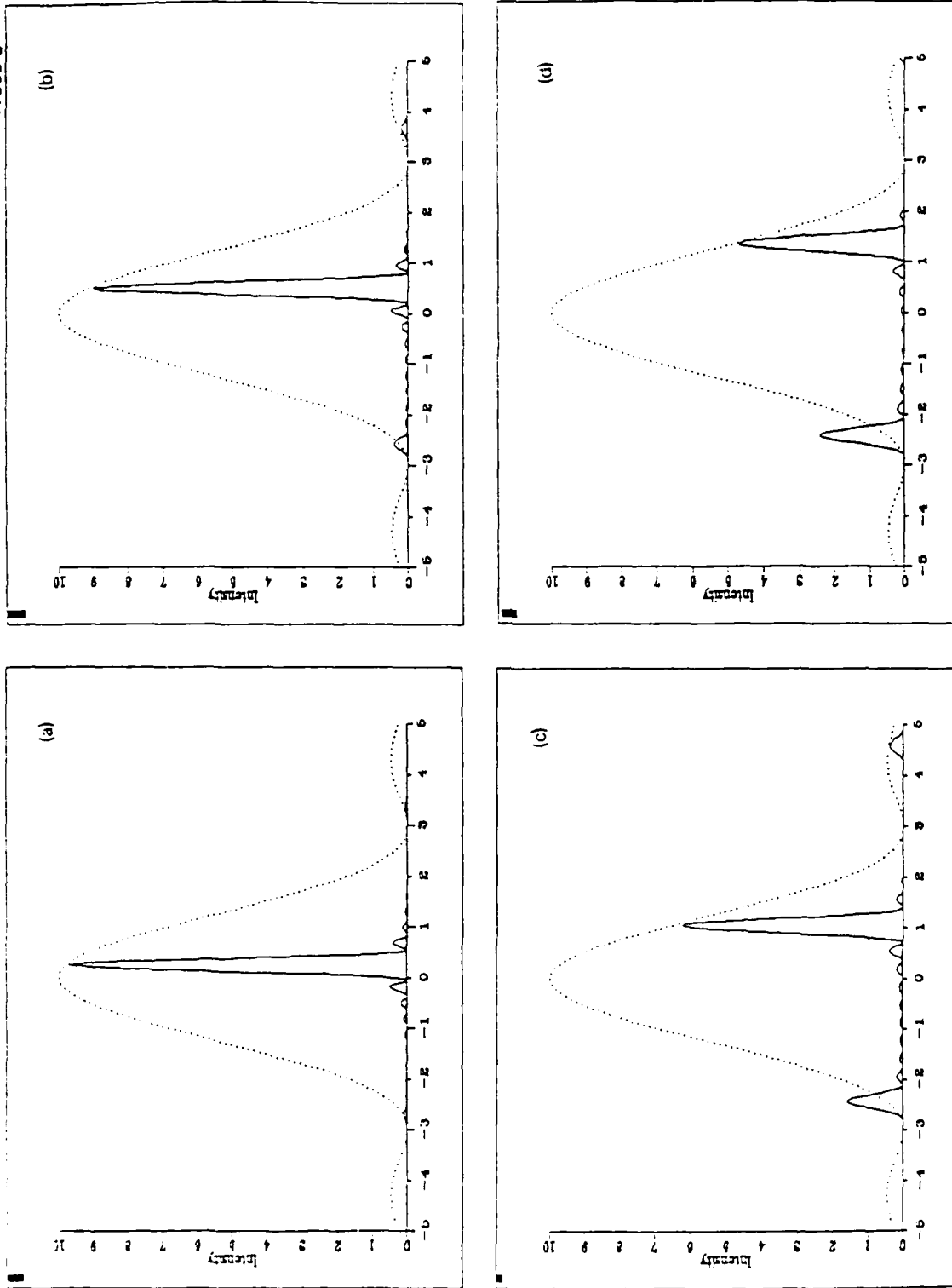


Figure 14. The transmitted beam may be steered to the right by progressively phase shifting the discrete elements of the array. At large steering angles, power in side lobes may exceed the main beam.

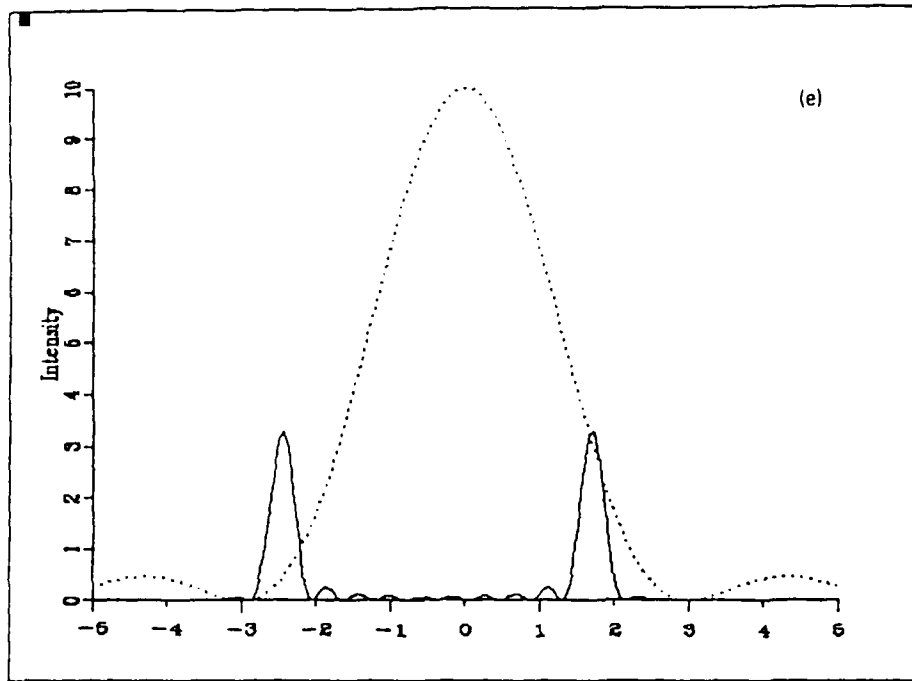


Figure 14. Continued.

The result of trying to phase steer by identically controlling patches of phase shifters is now clear. A patch of emitters, all with the same phase, is equivalent to a single larger element. It will have a proportionally narrower far-field beam pattern and narrower steering angle before side lobes become important. Patch phasing is not practical for large-angle steering. The implication for a discrimination system is that each phase shifter must be provided with a distinct phase adjustment signal which is different from its nearest neighbors.

Beam Focus Properties. Most radar systems employ fixed-focus antennas with the focal distance set at infinity. They radiate an initially collimated microwave beam which spreads due to diffraction effects. A typical radar beam width might be on the order of two degrees due to diffraction spreading.

Due to its very large antenna size, the decoy discrimination system can produce very narrow beams. The diffraction-limited beam width to the half-power points is given approximately by  $\lambda/D$  in radians. For an array diameter  $D$  of 10,000 m and a wavelength  $\lambda$  of 3 cm, the main-lobe beam width is approximately  $3 \times 10^{-6}$  radians or  $1.7 \times 10^{-4}$  degrees. A larger array can produce a proportionally smaller beam divergence. This diffraction spreading angle is considerably smaller than the angle subtended by the antenna at the target range. As seen from the target at a distance  $R$  of  $3 \times 10^6$  m, the antenna subtends an angle of  $D/R$  or  $3 \times 10^{-3}$  radians, which is 1,000 times greater than the beam spreading angle. The result is that the large transmitting antenna can produce a focused spot at range which is about 1,000 times smaller than its own diameter, or about 10 m diameter at its half-power points.

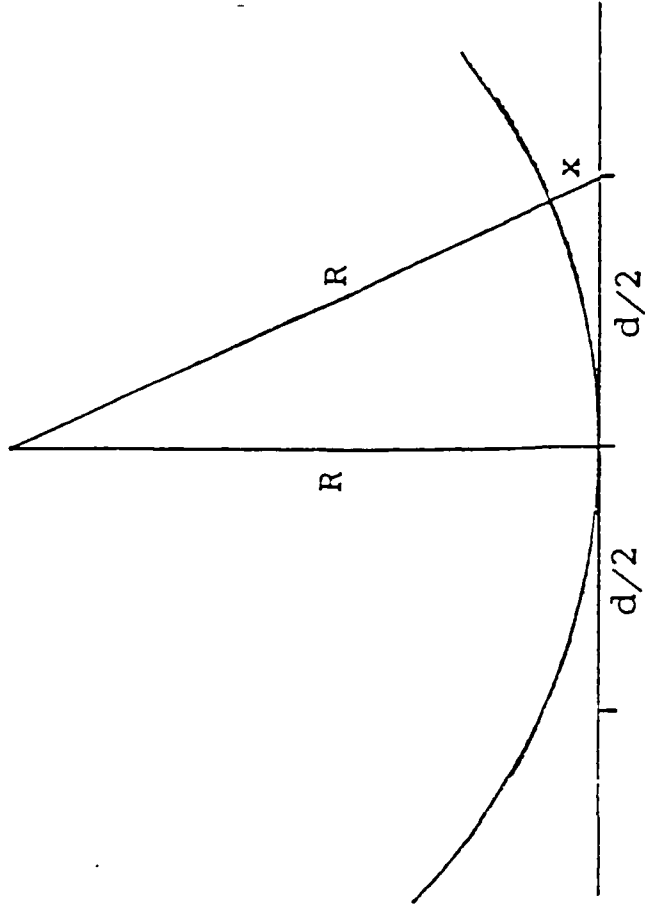
In order to produce a distant focused beam, the antenna must launch a converging wave. The wavefronts which leave the antenna must be aligned to a spherical surface whose center of curvature is located at the target. At great range, the curvature is very slight. The amount of phase correction required to deform a plane wave into the appropriate curved wave

plane wave into the appropriate curved wave changes very little between adjacent antenna elements. It may be very feasible to introduce such small phase corrections as constant shifts to large-area patches of the array.

Figure 15 illustrates the calculation of patch size for focusing purposes. A spherical converging wave may be approximated as a stepped series of flat wavefronts. Suppose  $x$  is the difference between the desired curved wave and a perfectly flat wave. If the wavefront error  $x$  can be kept less than  $1/10$  wavelength, the degradation in the far-field spot will be negligible compared to a perfectly smooth curved wave.

Degradation of the far-field Strehl ratio scales approximately as  $\cos^2(x/\lambda)$  or, in this case,  $\cos^2(0.1) = (0.995)^2 = 0.99$ . From Figure 15, it may be seen that the curved wave differs from a plane wave by an amount  $x$  for patch sizes larger than 268 m. This means that, in addition to phase tilts for beam-steering purposes, the array may be focused by applying additive uniform phase corrections to relatively large patches of the array. Focus is very important for the decoy discrimination system, and it is a fortunate simplification that the corrections may be applied in a simple additive fashion to large areas of the array.

Summary. Phased-array beam steering over more than  $60^\circ$  fields of view is practical for phase-shifter densities of one shifter per square wavelength in the transmitting aperture. If half-power beam steering to  $120^\circ$  is desired, then phase shifters must be spaced at  $1/2$  wavelength intervals for a density of four phase shifters per square wavelength. The feasibility of using dense shifter arrays is primarily an economic issue. If inexpensive printed circuit designs can be developed, there may be little cost difference between one and four shifters per square wavelength. In that case, the denser array will provide superior performance because of the lower level of side lobes at all steering angles.



For right triangles,

$$(d/2)^2 + R^2 = (R + x)^2$$

$$d^2/4 + R^2 = R^2 + 2Rx + x^2$$

$$d^2/4 = 2Rx + x^2$$

$$d^2 \approx 8Rx$$

LET  $x = \lambda/10 = 3 \times 10^{-3} \text{ m}, \quad R = 3 \times 10^6 \text{ m},$

THEN  $d^2 = 7.2 \times 10^4 \text{ m}^2, \quad d = 268 \text{ m}.$

Figure 15. For large ranges R, converging spherical wavefronts differ from plane waves by less than 1/10 wave over relatively large areas.

Beam steering requires linear phase tilt adjustments across the array. In general, each phase shifter will have a different phase setting than its neighbors, which means that phase adjustments cannot be applied in patches. This is not to say that phase adjustments must be continually variable analog corrections. Phase adjustments may be done in digitized steps as large as 1/4 wave at each shifter, as is practised in digitally steered search radars. However, any two adjacent shifters will require different step settings for some steering angles. Phasing in uniform patches is not practical.

Beam focus requires only very slight curvatures compared to plane wavefronts for the antenna sizes and target ranges of interest in a discrimination system. Spherical waves can be approximated by stepped plane waves with minimal far-field beam degradation if the wavefront error is kept to less than 1/10 of a wave. Relatively large patches can have the same focus adjustment, which means that separate focus commands are not required for each phase shifter.

#### **3.4.2 The Effects of Aperture Thinning and Phase Errors on a Large Phased-Array Antenna**

Ideally, the antenna for the ground-based HPM decoy discrimination system would consist of a nearly circular, uniformly filled and uniformly illuminated transmitting aperture. The purpose of the antenna is to launch a collimated or converging wave toward a distant target. In an ideal antenna system, the radiated wavefront would be perfectly smooth across the entire aperture; i.e., all portions of the antenna should be perfectly in phase and radiate with equal amplitude. A real antenna system, of course, will be subject to many compromises, all of which tend to degrade the maximum power density which can be projected to a target.

It is straightforward to calculate the far-field performance of a phased array antenna. Conceptually, the field at any distant point is simply the vector sum of the contributions from each radiating point at the antenna. In most cases, a large antenna will be constructed from many identical submodules, which can greatly simplify the calculational problem. The calculations presented here are due to R. Kwong, 1985 and 1986. They make maximum use of antenna symmetry and computationally efficient fast Fourier transform algorithms.

The calculations presented below are intended to answer two questions. First, what is the effect of thinning a phased array? A large array may be typically constructed from smaller modules which have some dead spaces or do not perfectly join together. Looking ahead, it is shown below that the amount of power in the main transmitted beam is reduced approximately by the fill factor of the phased array. For example, if the transmitting array has 10 percent void space between radiating subapertures, then approximately 10 percent of all transmitted power will go into side lobes instead of into the main beam.

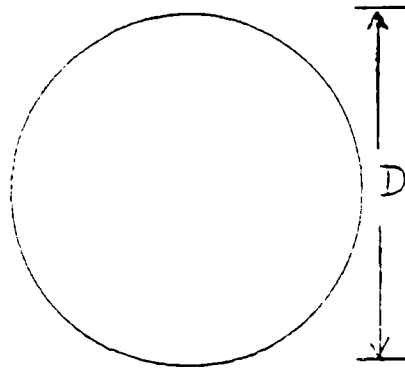
The second question considered below is the effect of antenna phase errors on the peak power at the target. It is shown that phase errors greater than about  $\lambda/10$  across significant portions of the antenna begin to seriously degrade the far-field performance.

Thinned Arrays. Consider the ideal case of a uniformly illuminated circular transmitting aperture of diameter  $D$ , shown in Figure 16 on top and designated  $S_1$  below. The far-field pattern (Fraunhofer limit) may be calculated in closed form and is proportional to a Bessel function of the first kind.

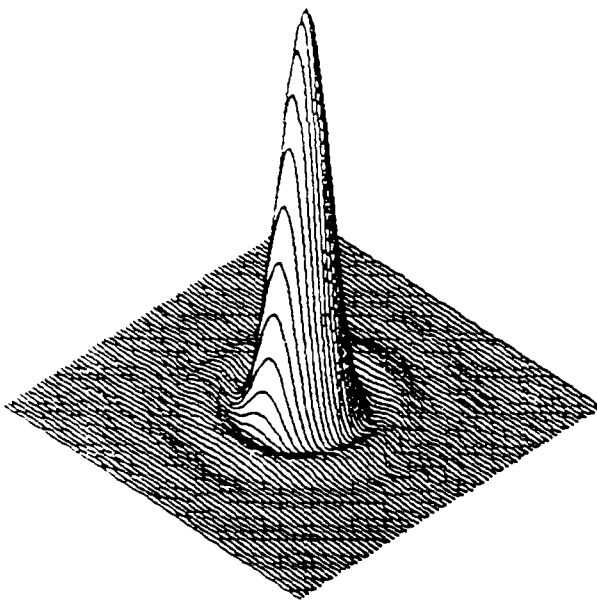
The irradiance pattern at a distant target for this well-known case is the familiar Airy pattern, shown in the lower part of Figure 16. It consists of a strong central peak surrounded by several weak bright and dark diffraction rings. The width of the central peak, i.e., its radius from the maximum to the first

17800-6

S1



S1



S1

17808-28

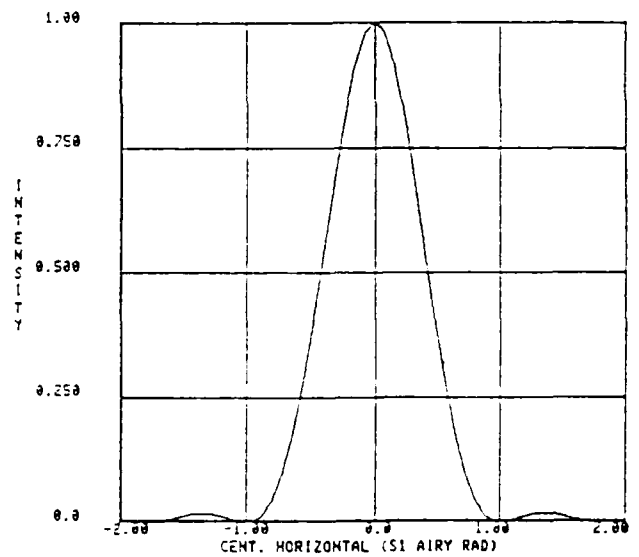


Figure 16. Irradiance pattern for uniformly illuminated circular aperture.

zero, is proportional to the range to the target times  $1.22 \lambda/D$ , as shown in the central-slice intensity plot. The central peak width also depends upon any focusing properties of the transmitting antenna.

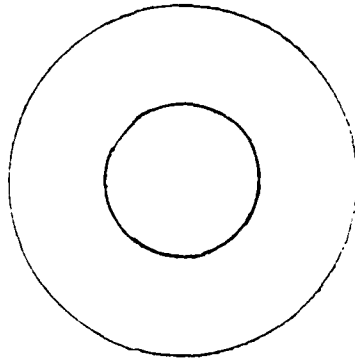
The power contained within the central peak amounts to 85% of the total transmitted power. All transmitted power which falls outside of the main central peak is usually referred to as side-lobe power. The shape of the peak and position of the zeroes of the diffraction pattern can be slightly altered by using nonuniform illumination across the aperture, but for most practical purposes S1 is the best performance that can be achieved. The most important feature to note is that large apertures  $D$  and short wavelengths  $\lambda$  produce small spots  $\lambda/D$  at the target.

Next compare the baseline performance of S1 to various thinned arrays. S1C (Figure 17) is a circular aperture with a large central obscuration. In the case shown, 40% of the transmitting aperture radius has been removed.

It is well known that a central obstruction can slightly increase the resolving power of an aperture. The width of the central or main lobe is clearly seen to be somewhat smaller than in the S1 case. However, the power in the main lobe is down and the side lobes have increased. In this case, approximately 50% of the total transmitted power is contained in the slightly narrower main lobe. The important point to note is that thinning the aperture has put more transmitted power into the side lobes.

Next consider the array of 64 small circular apertures designated S64 (Figure 18). The total illuminated area of S64 is identical to the area of S1. Due to the small spacings between subapertures, S64 has a slightly larger overall diameter than S1. For this reason, the main lobe of S64 is slightly narrower than S1. The peak main-lobe power of S64 is identical to S1, but the total power in the side lobes is larger. The effect of thinning

S1C  
(0.4 linear obscuration)



S1C

S1C

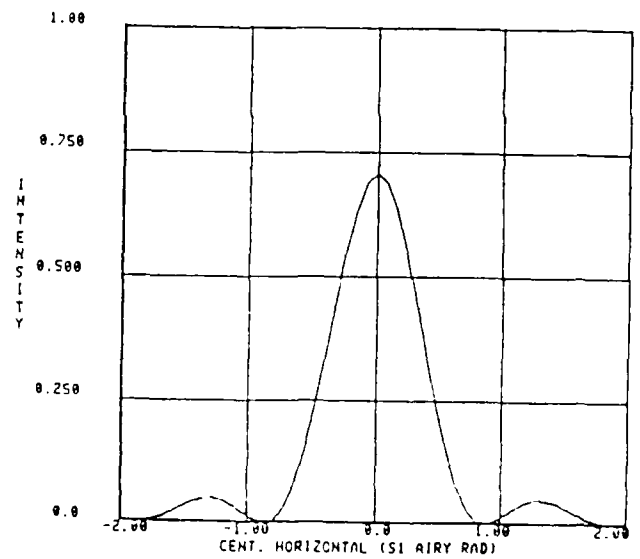
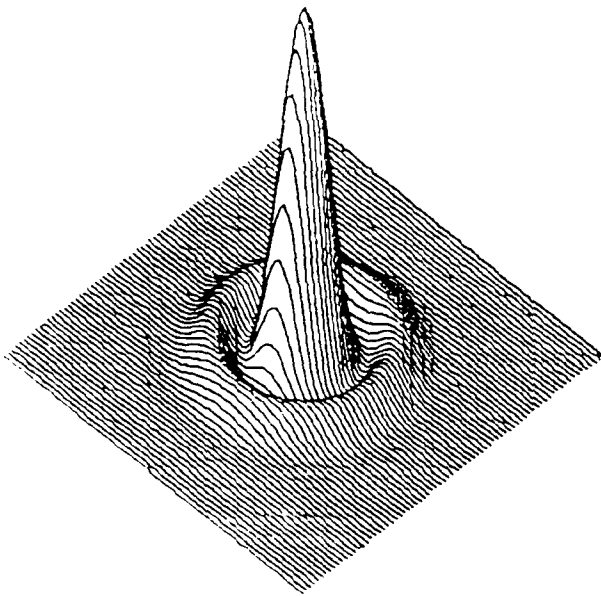
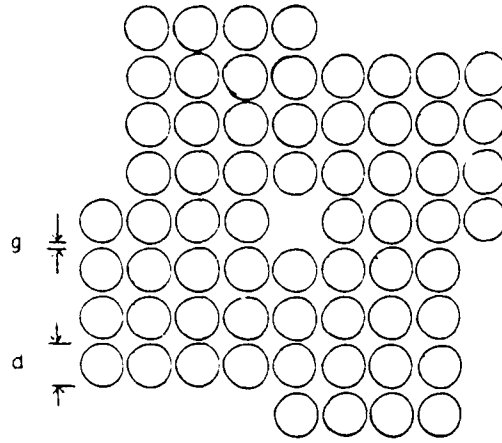


Figure 17. Irradiance pattern for centrally obscured circular aperture.

S64

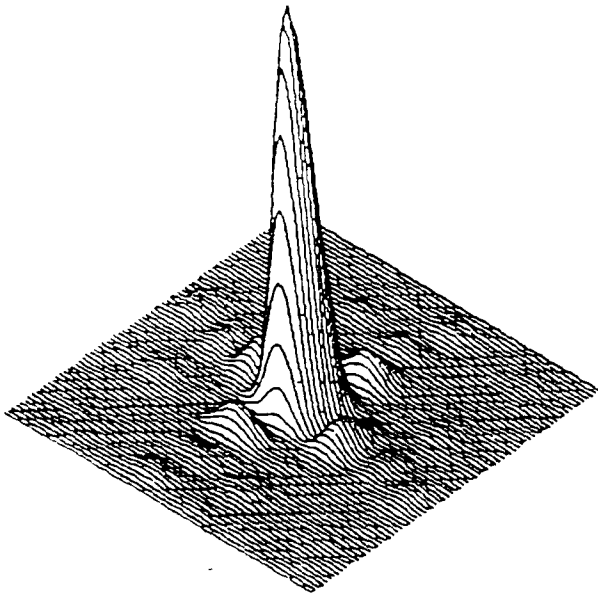
17808-30

$$a = D/8$$
$$g = a/10$$



17808-31

S64



S64

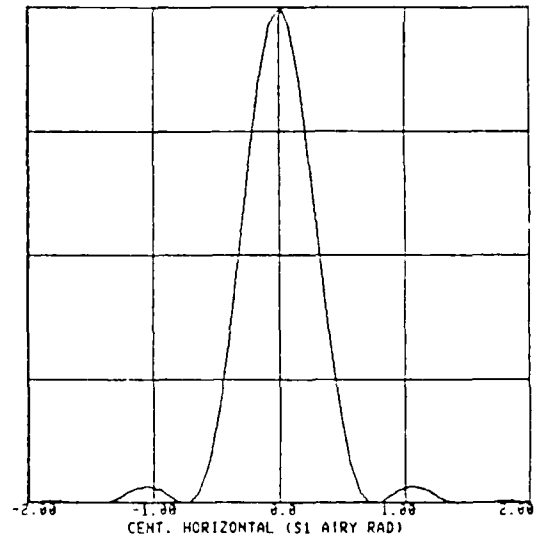
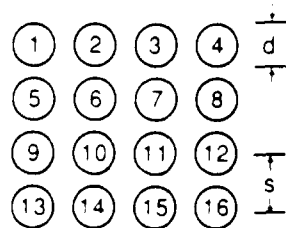


Figure 18. Array of 64 small circular subapertures.

has been to reduce the width of the main lobe and its total energy but not its peak power. Eliminating the circular symmetry has produced lumpy side lobes with rectangular symmetry in place of the smooth rings of S1.

The effects of array thinning can be seen more clearly in the simulations of far-field beam patterns from an array of 16 circular apertures, see Figure 19. With the ratio  $s/d = 1$ , the subapertures just touch each other. The far-field intensity pattern in Figure 20 shows a single strong main lobe which is nearly identical to the filled circular-aperture case S1. As the subaperture separation is increased, the main-lobe peak intensity remains the same; but the main-lobe width and total power in the lobe go down. Increased spacing or thinning leads to a larger fraction of the total power distributed among increasingly strong side lobes.

The above computer calculations demonstrate a simple scaling law for thinned arrays. The peak power in the main lobe of a perfectly phased array is proportional to the total illuminated area of the array and is independent of the shape or fill factor of the array. The width of the main lobe, however, is inversely



C17808-38

CASE	SUBAPERTURE PHASE SHIFTS (PISTON ONLY)
A	DIFFRACTION-LIMITED
B	$\phi_1 = \phi_3 = \phi_6 = \phi_8 = \phi_9 = \phi_{11} = \phi_{14} = \phi_{16} = p$ $\phi_2 = \phi_4 = \phi_5 = \phi_7 = \phi_{10} = \phi_{12} = \phi_{13} = \phi_{15} = -p$ WITH $p = \lambda/40$
C	SAME AS B BUT WITH $p = \lambda/20$
D	SAME AS B BUT WITH $p = \lambda/10$

Figure 19. Array of 16 circular subapertures.

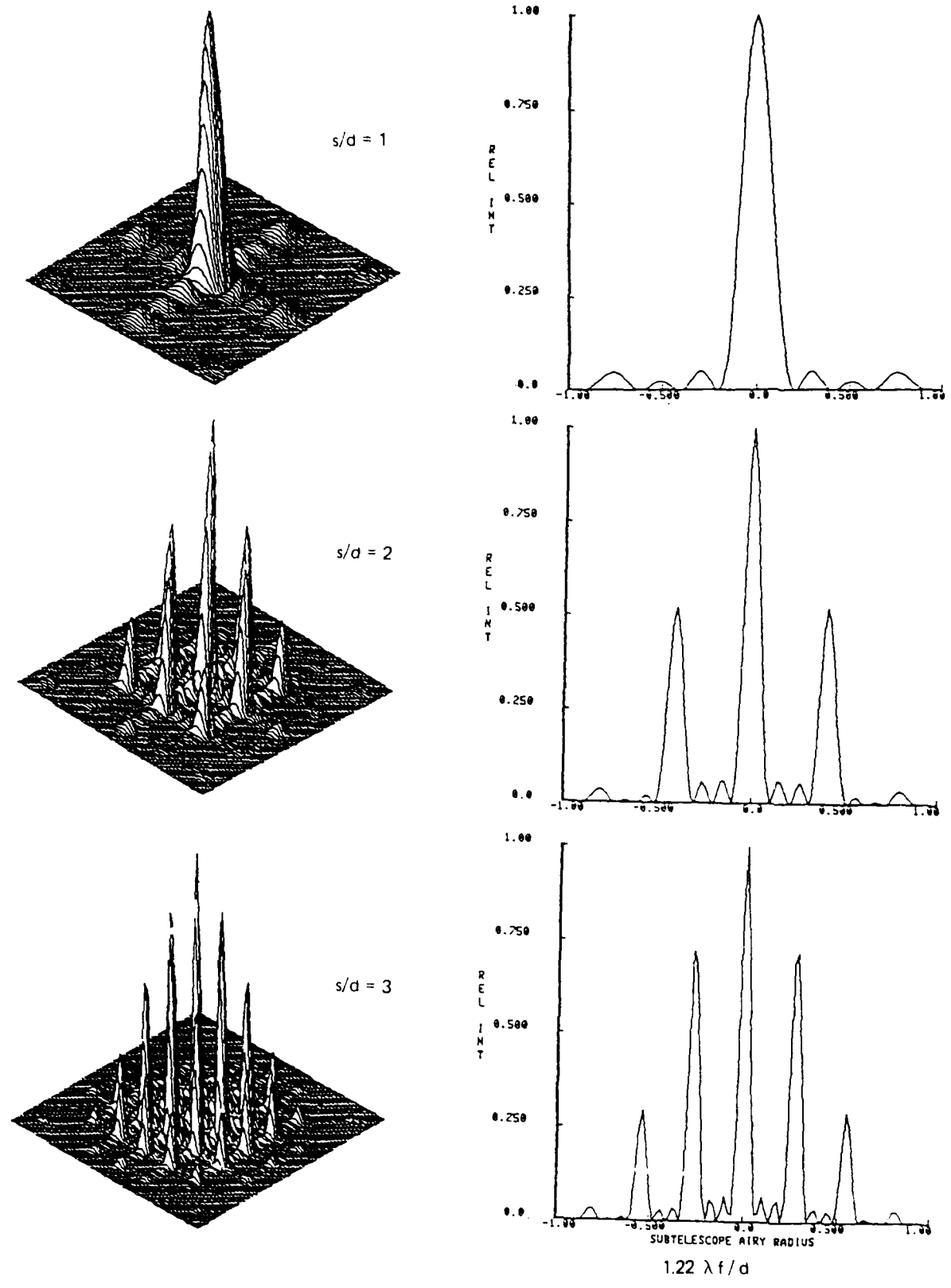


Figure 20. Far-field patterns of case A (diffraction-limited).

power in the main lobe (integral of power over main lobe area) is a fraction of the total transmitted power and, in fact, is given simply by the array fill factor:

$$P (\text{main lobe}) = P (\text{filled-array main lobe}) \times \text{Fill Factor}. \quad (15)$$

For example, if the array is 90% filled, then an additional 10% of the total transmitted power will be scattered from the main beam to side lobes. A proof of this scaling law is available in analytical closed form (see R. Pringle, 1987).

Phase Errors in Arrays. The above calculations of far-field intensities have assumed that all elements of the array were radiating with perfectly correct phases. Using the 16-element square array, it is a straightforward matter to introduce phase differences between the elements. Figures 21 through 23 illustrate the degradation due to phase errors which alternate from plus to minus  $\lambda/N$  between adjacent subapertures, where  $N = 40, 20,$  and  $10,$  respectively.

It is apparent that phase errors less than  $\pm \lambda/20$  between adjacent subapertures are insignificant. Phase errors larger than  $\pm \lambda/10$  cause a significant decrease in the main-lobe peak power and an increase in the total power scattered to side lobes. A reasonable design goal for phased-array antennas is to maintain rms phase errors to less than  $\lambda/10$ . For a 3-cm wavelength corresponding to 10 GHz, the antenna surface figure should be held either mechanically or electrically accurate to 3 mm.

Summary. Array thinning has no effect on the peak power at the center of the main beam, but it significantly scatters power into side lobes. For a given total transmitter power and active antenna area, the factor by which the total power in the main beam is reduced is precisely the fill factor of the array.

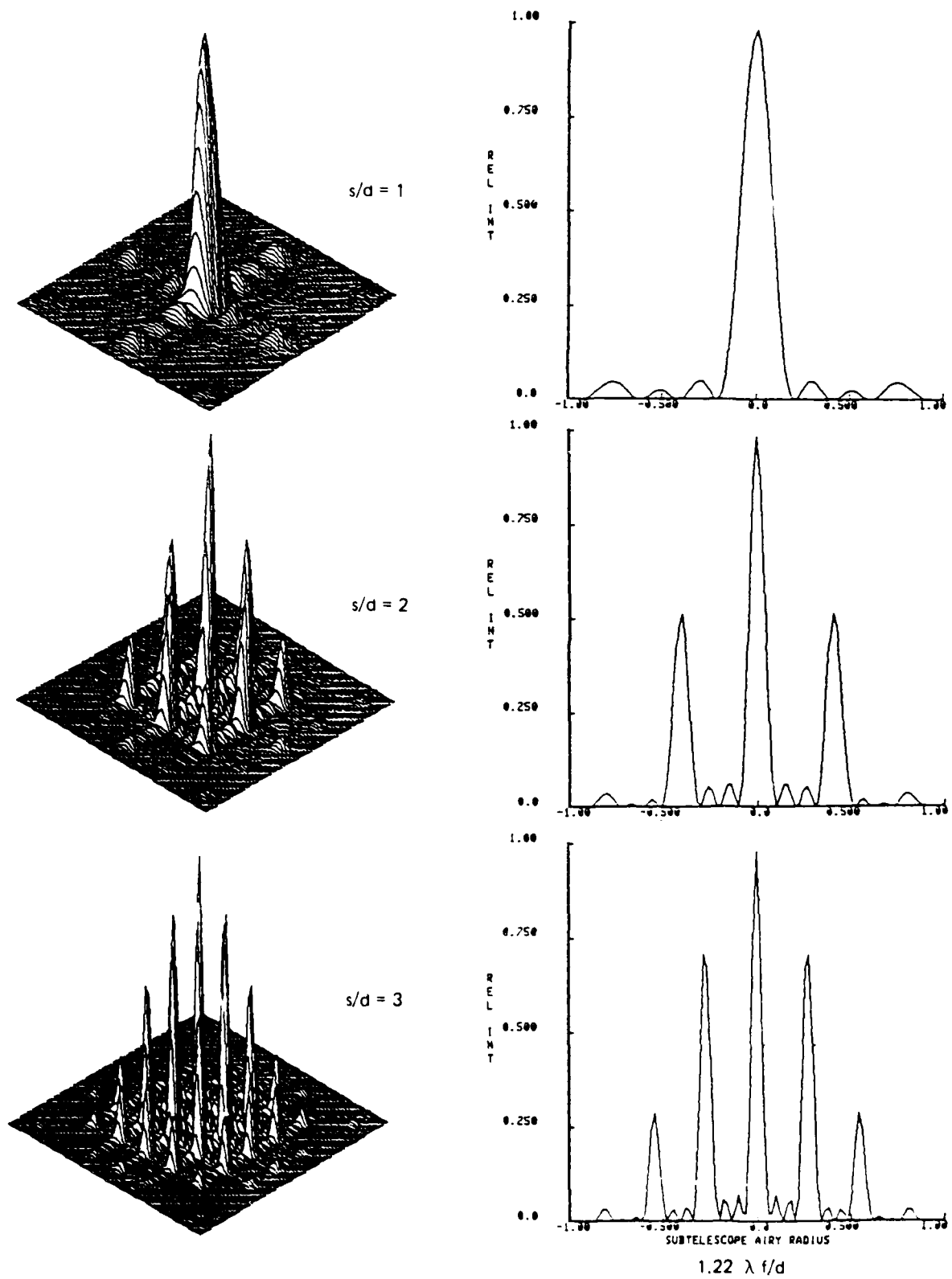


Figure 21. Far-field patterns of case B ( $\lambda/40$  piston).

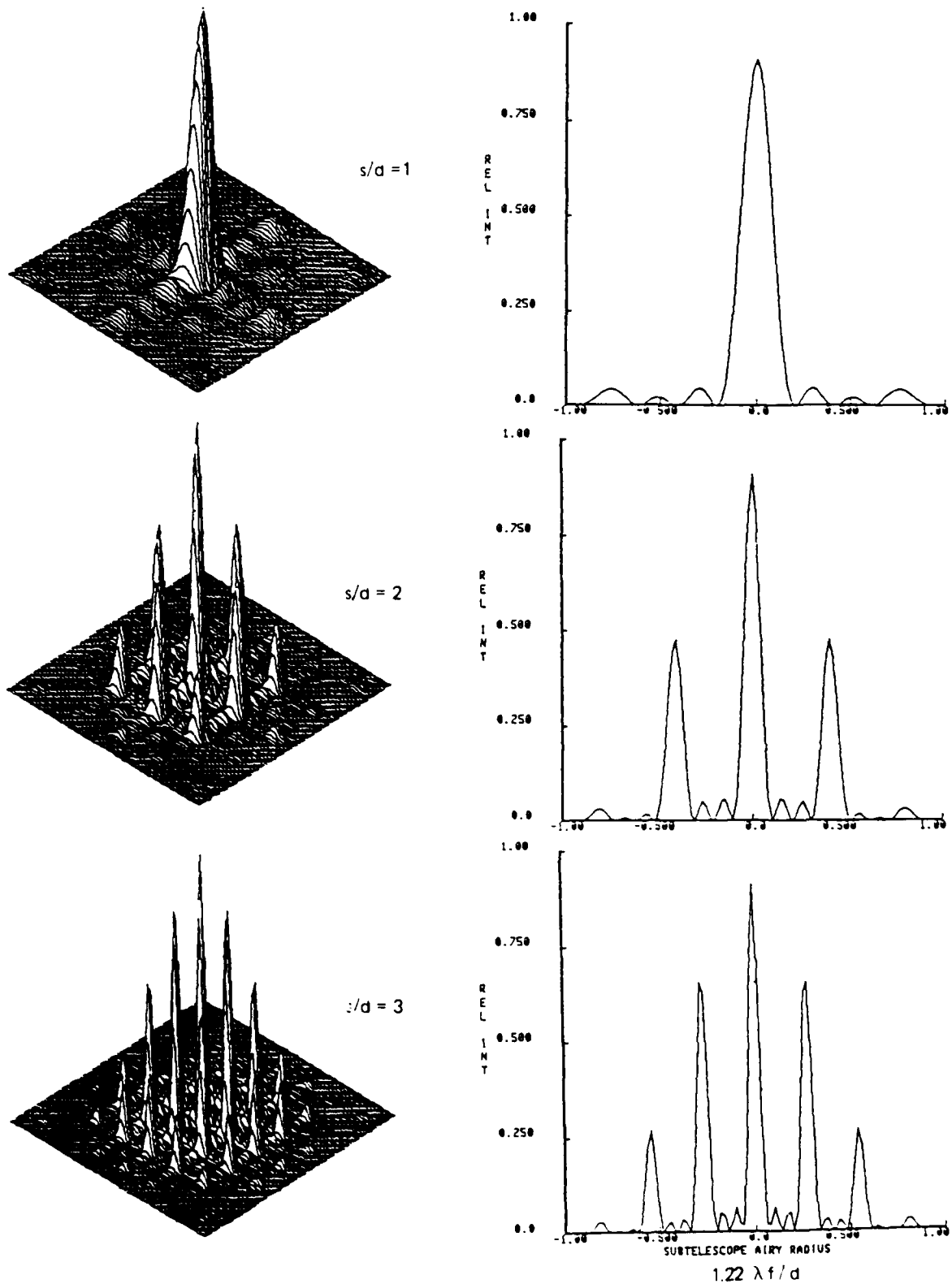
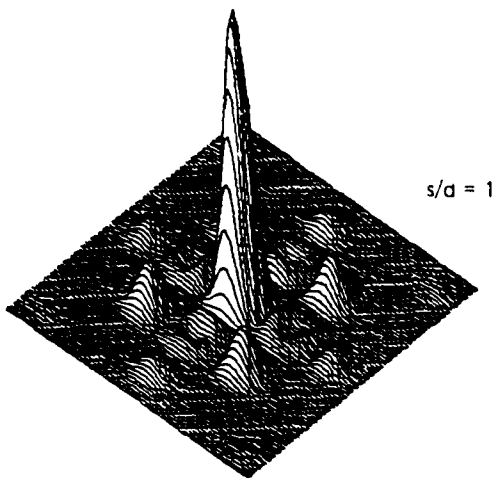
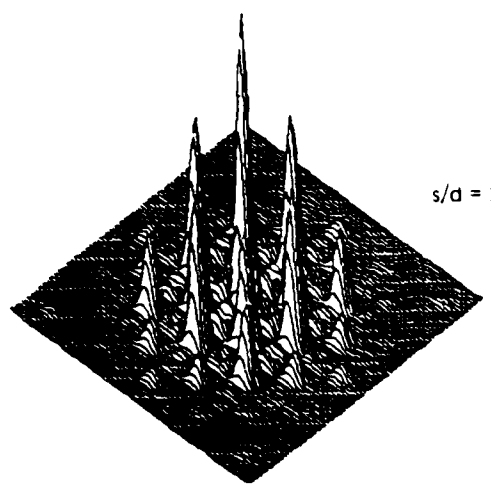
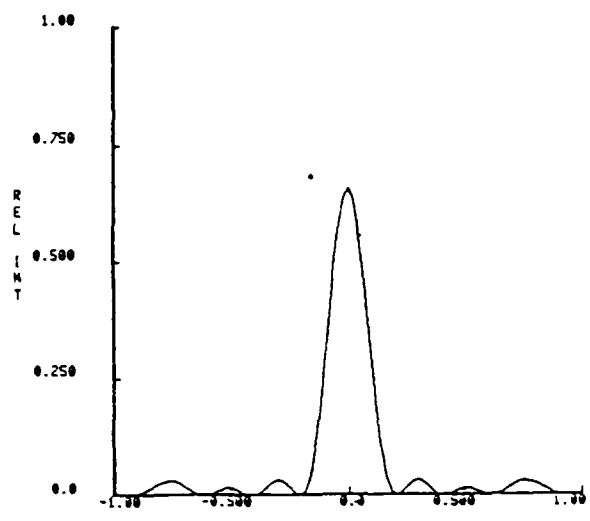


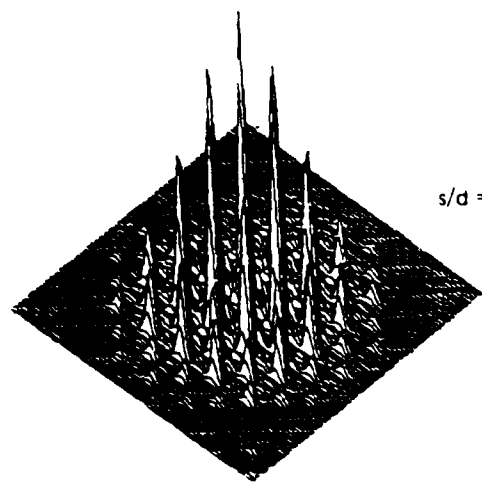
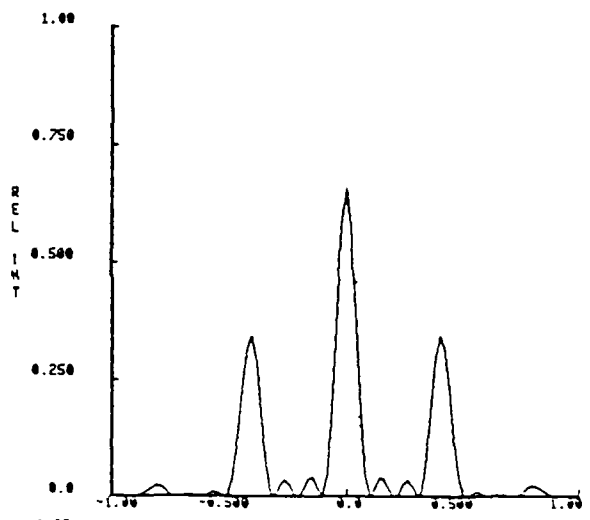
Figure 22. Far-field patterns of case C ( $\lambda/20$  piston).



s/d = 1



s/d = 2



s/d = 3

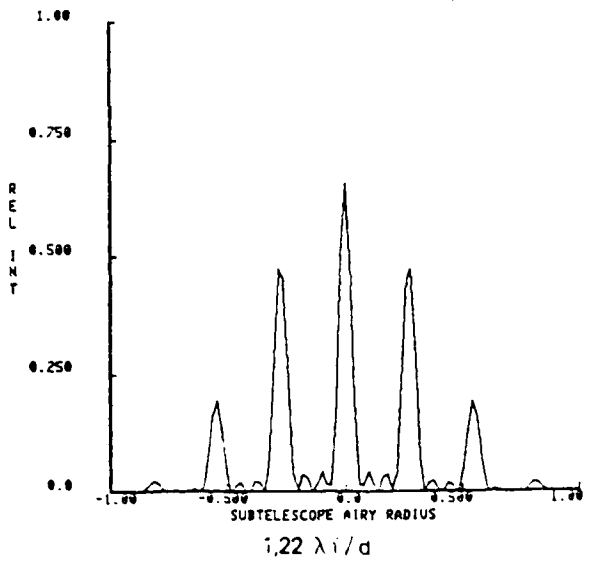


Figure 23. Far-field patterns of case D ( $\lambda/10$  piston).

Spreading out an array of subapertures has the effect of narrowing the main beam and scattering more power into side lobes. An HPM discrimination system should probably be designed for a fill factor approaching 80%. A rectangular close-packed array of circular apertures, as illustrated above, has a fill factor of  $\pi/4 = 0.785$ , which would probably be satisfactory.

Phase errors between subapertures degrade most aspects of a phased array. Both the peak power in the main beam and the total power in the main beam are reduced while power in the side lobes increases. Degradation effects become significant with phase errors larger than  $\lambda/10$ .

### **3.5 TASKS 17 - 18: HIGH-POWER PHASE-SHIFTER CONCEPT EXPLORATION**

#### **3.5.1 Phase-Shifter Arrays**

Having established that: 1) beam steering over  $60^\circ$  requires phase-shifter densities at least as high as one phase shifter per square wavelength, and that 2) sidelobe suppression requires a highly filled array, it is clear that a very large number of phase shifters will be required. Current waveguide phase-shifter technology is costly and would easily dominate the total system costs. A simpler and less expensive concept is required. The following calculations estimate the magnitude of phase shifts which might be achievable from arrays of simple resonant loops and dipoles. The results initially look practical and promising.

Consider a resonant LRC loop (Figure 24) as a candidate phase-shifting element. The loop will couple more or less strongly to an incident electromagnetic radiation field depending upon its resonant frequency and its internal losses or  $Q$ .

An array or planar sheet of resonant loops (Figure 25) can be used to retard the phase of a plane wave in transmission. If the array is placed before a flat reflecting surface, phase shifts can be obtained in reflection by a double pass through the array (Figure 26).

17808-7

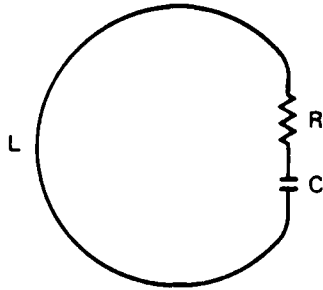


Figure 24. Resonant loop.

17808-8

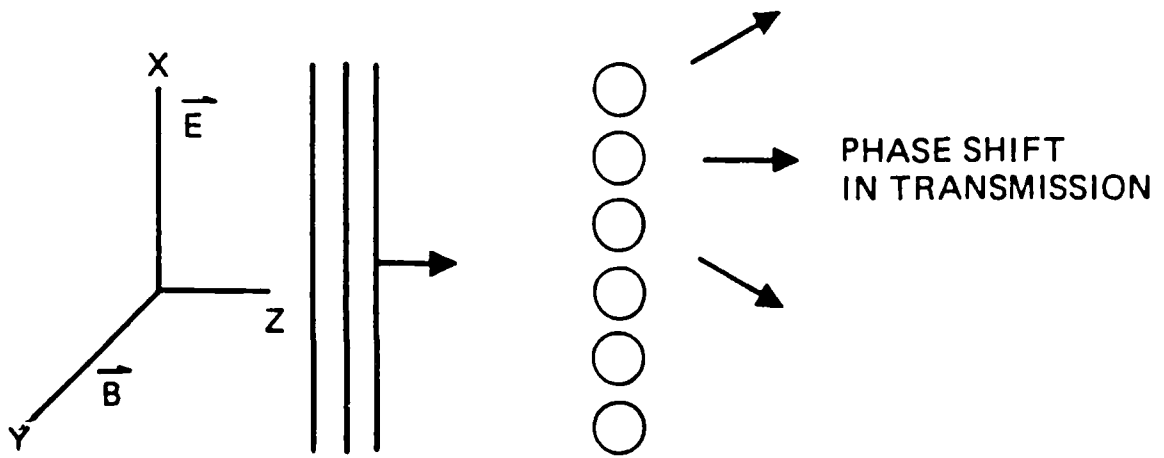


Figure 25. Array of resonant loops.

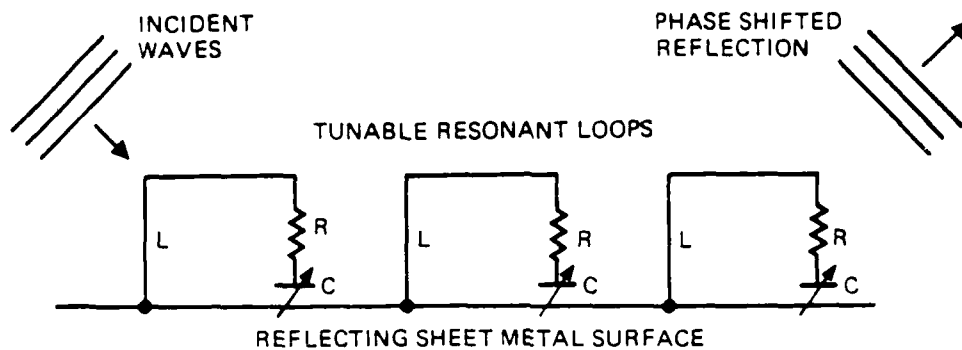


Figure 26. Phase shift in reflection.

The calculation of phase shift versus resonant-loop tuning will proceed in five steps:

- 1) Using Faraday's induction law, estimate the voltage induced in a loop due to an incident plane-wave field.
- 2) Consider the loop as a nearly resonant harmonic oscillator. Estimate the steady-state oscillating current induced in the loop due to the driving voltage calculated in (1) above.
- 3) Develop an expression for the dipole radiation field from a loop with a steady-state oscillating current.
- 4) Consider a plane wave incident upon a sheet array of identical resonant loops. After transmission through the array, the resulting field will be a vector sum of the attenuated incident field and the field scattered by the array. Compare this sum field to a time-delayed plane wave, as if it had passed through a material with some index of refraction and thickness.
- 5) Estimate the number of waves of phase retardation for some typical loop dimensions and operating frequencies.

Step 1: Faraday's Induction Law. Consider a single-frequency plane wave incident upon an LRC loop. Rationalized MKS units will be used throughout these calculations in order to relate the results to easily measured quantities. In the usual convention, measurable quantities are taken as the real part of complex expressions. Consider first a summary of the properties of plane waves.

Incident fields:

$$\vec{E} = \hat{x} E_0 e^{i(kz - \omega t)} \quad (16)$$

$$\vec{B} = \hat{y} B_0 e^{i(kz - \omega t)} \quad (17)$$

$$k = \frac{\omega}{c}$$

For plane waves in free space:

$$\nabla \times \vec{E} = - \frac{\partial \vec{B}}{\partial t} \quad (18)$$

$$\frac{\partial E_x}{\partial z} = - \frac{\partial B_y}{\partial t}$$

$$ikE_0 = i\omega B_0$$

$$B_0 = \frac{k}{\omega} E_0 = \frac{1}{c} E_0 = \sqrt{\epsilon_0 \mu_0} E_0 \quad (19)$$

Power flow from Poynting's vector:

$$\vec{S} = \vec{E} \times \vec{H} = \vec{E} \times \vec{B} / \mu_0 \quad (20)$$

$$|\vec{S}|_{\text{average}} = \frac{1}{2} E_o \frac{\sqrt{\epsilon_o \mu_o}}{\mu_o} E_o = \frac{1}{2} \sqrt{\frac{\epsilon_o}{\mu_o}} E_o^2 \quad (21)$$

Next consider the voltage induced in a loop due to a time-varying magnetic field aligned normal to the plane of the loop, given by Faraday's induction law. Since a small loop antenna couples to the magnetic field rather than to the electric field, it is convenient to perform most of the following calculations with the magnetic components of the electromagnetic wave. The induced loop voltage (Figure 27) will serve as the driving voltage for oscillating currents in the loop.

Induced Voltage:

$$\begin{aligned} V_{\text{Drive}} &= \oint \vec{E} \cdot d\vec{l} & (22) \\ &= - \frac{d}{dt} \iint \vec{B} \cdot d\vec{s} \\ &= - \frac{d}{dt} B A_{\text{Loop}} \\ &= i \omega A_{\text{Loop}} B_o e^{-i\omega t} \end{aligned}$$

$$\text{Let } V_{\text{Drive}} \equiv V_D e^{-i\omega t}, \text{ then } V_D = i \omega A_{\text{Loop}} B_o \quad (23)$$

Step 2: Driven Harmonic Oscillations. An LRC series loop may be modeled by a linear differential equation which is derived from Kirchhoff's voltage law around the loop (Figure 28):

$$V_{\text{Drive}} = V_L + V_R + V_C, \quad V_L = L \frac{dI}{dt}, \quad V_C = C \frac{dV_C}{dt} \quad (24)$$

17808-11

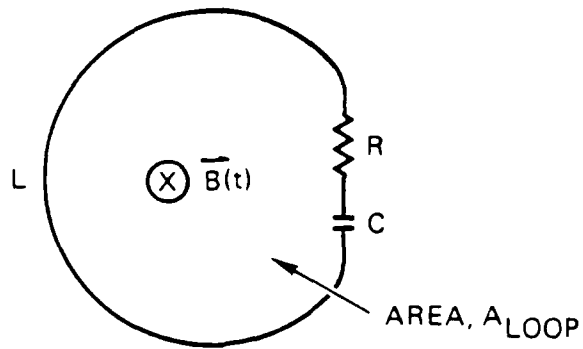


Figure 27. Loop in B-field.

17808-12

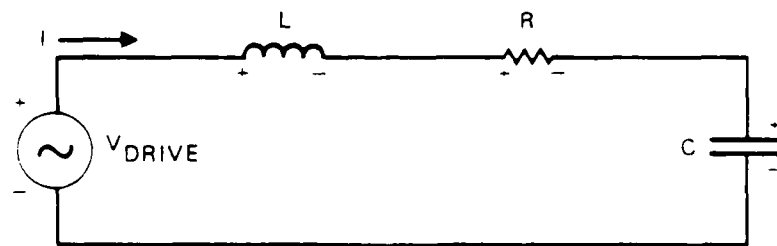


Figure 28. Voltage-driven loop.

$$V_{\text{Drive}} = L \frac{dI}{dt} + IR + \frac{1}{C} \int I dt$$

$$\dot{V}_{\text{Drive}} = L \ddot{I} + R \dot{I} + \frac{1}{C} \dot{I}$$

Assume:

$$V_{\text{Drive}} = V_D e^{-i\omega t} \quad (V_D \text{ complex}) \quad (25)$$

$$I = I_0 e^{-i\omega t} \quad (I_0 \text{ complex}) \quad (26)$$

Forced loop oscillations:

$$-i\omega V_D = -\omega^2 L I_0 - i\omega R I_0 + \frac{1}{C} I_0 \quad (27)$$

$$i\omega V_D = (\omega^2 L - \frac{1}{C}) I_0 + i\omega R I_0$$

$$I_0 = \frac{i\omega V_D}{(\omega^2 L - \frac{1}{C}) + i\omega R} = \frac{V_D}{R + \frac{1}{i\omega} (\omega^2 L - \frac{1}{C})}$$

$$= \frac{V_D}{R - \frac{iL}{\omega} (\omega^2 - \frac{1}{LC})} \quad , \quad \omega_0^2 \equiv \frac{1}{LC}$$

$$= \frac{V_D}{R - \frac{iL}{\omega} (\omega_0^2 - \omega^2)} \quad (28)$$

The steady-state loop current depends upon the magnitude of the driving voltage, the loop resistance or  $Q$  factor, and the detuning from resonance.

Step 3: Fields Radiated by an Oscillating Current Loop. The magnitude of the magnetic moment  $\vec{m}$  of the loop (Figure 29) is given by

$$|\vec{m}| = A_{\text{Loop}} I = A_{\text{Loop}} I_0 e^{-i\omega t} . \quad (29)$$

17808-13

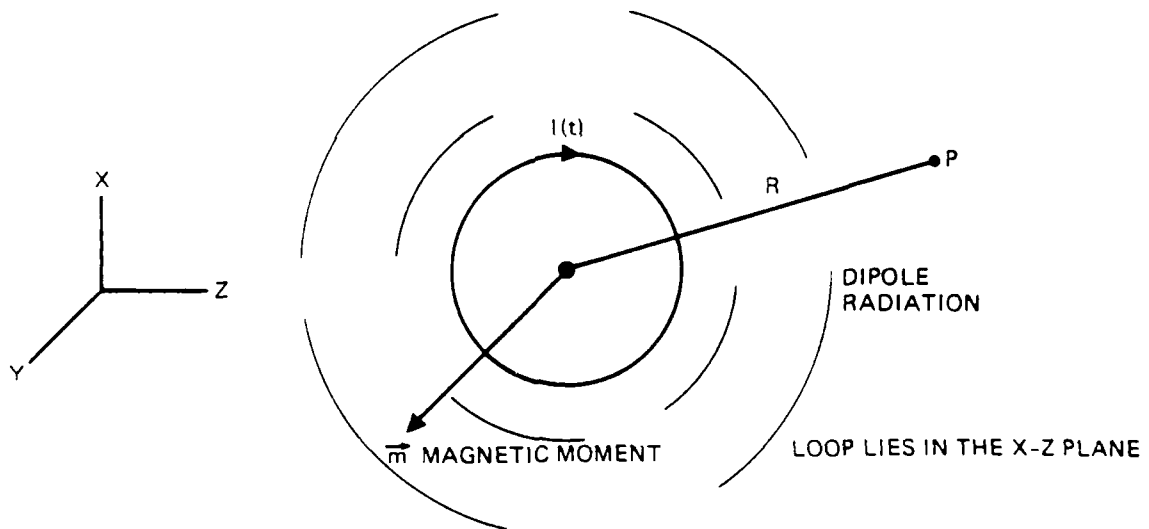


Figure 29. Magnetic moment of loop.

From Panofsky & Phillips, first edition Eq. (13-69), or second edition Eq. (14-92):

$$\vec{B}(\mathbf{R}) = \frac{i\mu_0 k^2 e^{ikR}}{4\pi R^3} [\vec{R} \times (\vec{m} \times \vec{R})] \quad (30)$$

Consider the magnetic field of the scattered dipole radiation (Figure 30):

$$|\vec{B}_{\text{scattered}}|_{\text{max}} = \frac{i\mu_0 k^2 e^{ikR}}{4\pi R} A_{\text{Loop}} I_0 e^{-i\omega t} ; \quad (31)$$

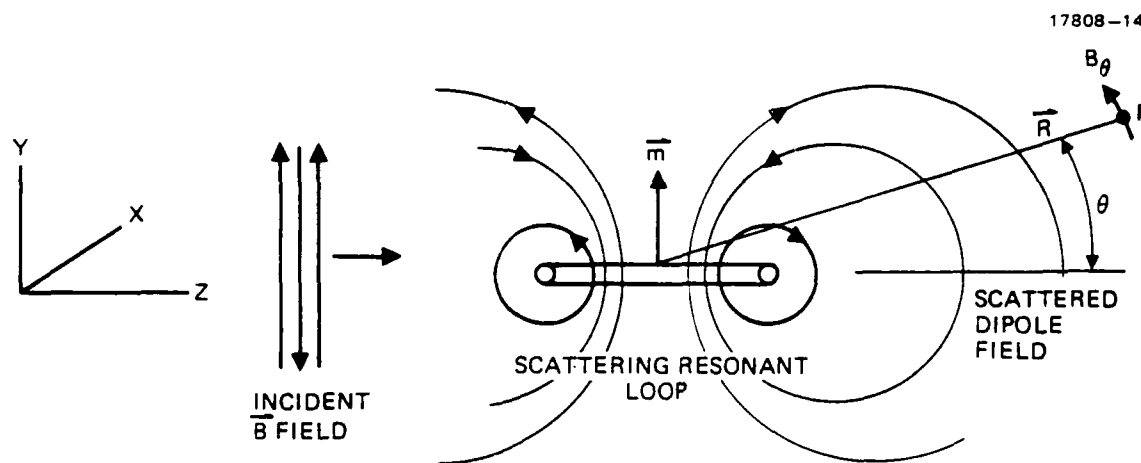


Figure 30. Scattered dipole field.

in the Y-Z plane (plane of the drawing),

$$B_{\theta}(r,t) = \frac{i\mu_0 \omega^2 A_{\text{Loop}} I_0}{4\pi c^2 r} \cos\theta e^{i(kr - \omega t)} \quad (32)$$

Step 4: Index of Refraction of an Array of Resonant Loops.

Consider a sheet of magnetic dipoles (Figure 31) which are driven in-phase by an incident wave. We want to calculate the field due to the sheet at point P.

Far from the sheet,  $\cos \theta \approx 1$ . The field at P may be found by summing the contributions from all of the dipoles. Each ring (Figure 32) contributes  $(2\pi\rho dp)N_A$  dipoles, where  $N_A$  = the number of dipoles/unit area.

The total field due to the sheet of dipoles:

$$B(z)_{\text{Dipole Sheet}} = \int_0^{\infty} N_A B(r,t) 2\pi\rho dp \quad (33)$$

We change the integration variable:

$$r^2 = \rho^2 + z^2 \quad ,$$

$$2r dr = 2\rho dp \quad , \quad \text{then}$$

$$B(z)_{\text{Dipole Sheet}} = \int_z^{\infty} \frac{N_A i\mu_0 \omega^2 A_{\text{Loop}} I_0}{4\pi c^2 r} e^{i(kr - \omega t)} 2\pi r dr \quad (34)$$

$$= \frac{iN_A \mu_0 \omega^2 A_{\text{Loop}} I_0}{2c^2} \int_z^{\infty} e^{i(kr - \omega t)} dr$$

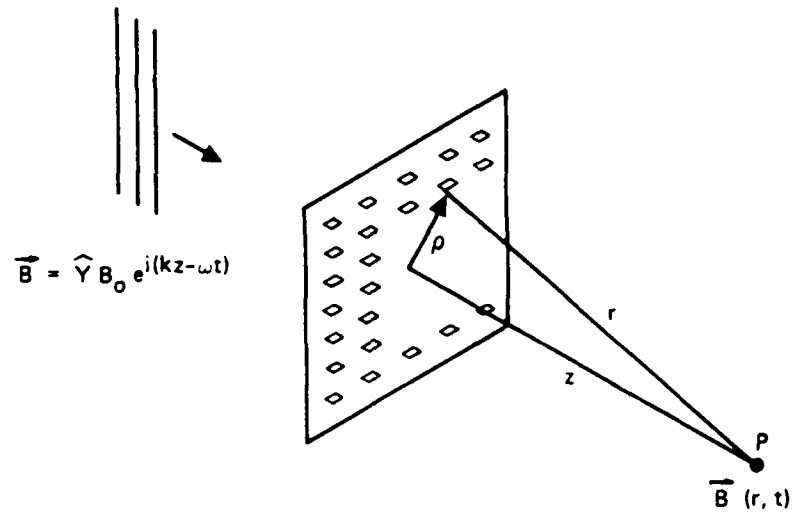


Figure 31. Sheet of magnetic dipoles.

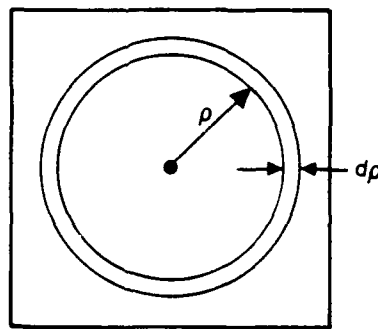


Figure 32. A ring of dipoles.

$$\begin{aligned}
\text{B(z)} &= \frac{i N_A \mu_o \omega^2 A_{\text{Loop}} I_o}{2c^2} e^{-i\omega t} \int_z^\infty e^{i \frac{\omega}{c} r} dr \\
\text{Dipole} & \\
\text{Sheet} & \\
&= \frac{i N_A \mu_o \omega^2 A_{\text{Loop}} I_o}{2c^2} e^{-i\omega t} i \frac{c}{\omega} \left( e^{i\infty} - e^{i \frac{\omega}{c} z} \right)
\end{aligned}$$

Here,  $N_A I_o e^{i\infty} = 0$ , because  $N_A \rightarrow 0$  and  $I_o \rightarrow 0$  for  $\rho \rightarrow \infty$  in any

real physical system. Thus,

$$\begin{aligned}
\text{B(z)} &= \frac{N_A \mu_o \omega A_{\text{Loop}} I_o}{2c} e^{i(kz - \omega t)} \\
\text{Dipole} & \\
\text{Sheet} &
\end{aligned} \tag{35}$$

Now put in  $I_o$  and compare to the expression for the incident B field. From Eq. (28),

$$\begin{aligned}
\text{B(z)} &= \frac{N_A \mu_o \omega A_{\text{Loop}}}{2c} \frac{V_D}{[R + i \frac{L}{\omega} (\omega_o^2 - \omega^2)]} e^{i(kz - \omega t)} \\
\text{Dipole} & \\
\text{Sheet} &
\end{aligned} \tag{36}$$

Using  $V_D$  from Eq. (23),

$$\begin{aligned}
\text{B(z)} &= \frac{N_A \mu_o \omega A_{\text{Loop}}}{2c} \frac{i\omega B_o A_{\text{Loop}}}{[R + i \frac{L}{\omega} (\omega_o^2 - \omega^2)]} e^{i(kz - \omega t)} \\
\text{Dipole} & \\
\text{Sheet} &
\end{aligned}$$

$$\vec{B}(z)_{\text{Dipole Sheet}} = \hat{y} \frac{iN\mu_o\omega^2}{2c} \frac{A_{\text{Loop}}^2}{[R + i\frac{L}{\omega}(\omega_o^2 - \omega^2)]} B_o e^{i(kz - \omega t)} \quad (37)$$

Note the phase shift  $i$  with respect to the incident wave,

$$\vec{B} = \hat{y} B_o e^{i(kz - \omega t)}.$$

Now estimate the index of refraction. Suppose the incident wave had passed not through a scattering dipole sheet (Figure 33), but through a material with index of refraction  $n$  and thickness  $\Delta z$  (Figure 34).

Inside the material, the wave velocity  $v = c/n$ . The additional time required to pass through the material is

$$\Delta t = (n - 1) \frac{\Delta z}{c}.$$

Thus, after passing through the material,

$$B_{\text{after}} = B_o e^{i[kz + (n - 1)\frac{\omega}{c} \Delta z - \omega t]}.$$

Set this expression = transmitted + scattered fields:

$$B_o' e^{i(kz - \omega t)} + B(z)_{\text{Dipole Sheet}} = e^{i\omega(n - 1)\Delta z/c} B_o e^{i(kz - \omega t)} \quad (38)$$

Transmitted Wave

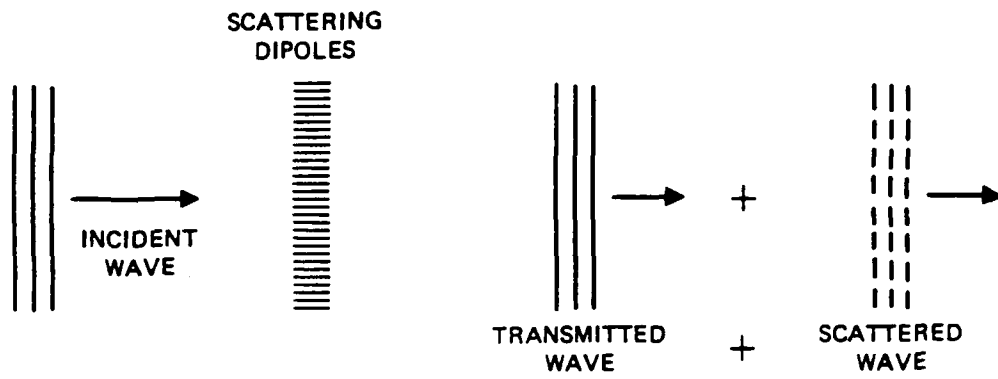


Figure 33. Scattering by dipole sheet.

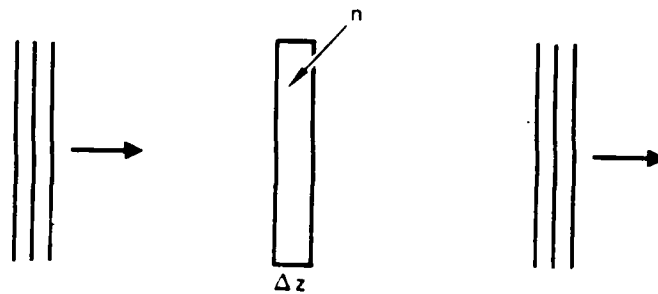


Figure 34. Delay by dielectric layer.

Note a simplifying assumption: Assume that the incident wave is transmitted by the dipole sheet without loss and that it adds coherently to the wave scattered from the dipole array:  $B'_o = B_o$ . This assumption will be approximately correct when the scattered wave amplitude is small compared to the incident wave. This approach assumes that the dipole sheet will make only a small change to the transmitted wave, which would be the case for a sufficiently thinned array of dipoles. An exact expression without this assumption requires an iterative solution. For  $n \approx 1$ , we can simplify  $B_{sct}$ . This approximation also assumes that the dipole sheet has only a small effect on the transmitted wave. Thus,

$$e^{i\omega(n-1)\Delta z/c} \approx 1 + i\omega(n-1)\frac{\Delta z}{c} + \dots$$

$$[1 + i\omega(n-1)\frac{\Delta z}{c}] B_o e^{i(kz - \omega t)} \approx B_o e^{i(kz - \omega t)} + \underset{\text{Dipole Sheet}}{B(z)}$$

$$i\omega(n-1)\frac{\Delta z}{c} B_o e^{i(kz - \omega t)} \approx \frac{iN A \mu_o \omega^2}{2c} \frac{A_{Loop}^2}{[R + i\frac{L}{\omega}(\omega_o^2 - \omega^2)]} B_o e^{i(kz - \omega t)}$$

$$\omega(n-1)\frac{\Delta z}{c} \approx \frac{N A \mu_o \omega^2}{2c} \frac{A_{Loop}^2}{[R + i\frac{L}{\omega}(\omega_o^2 - \omega^2)]}$$

$$n-1 \approx \frac{N_A}{\Delta z} \frac{\mu_o \omega}{2} \frac{A_{Loop}^2}{[R + i\frac{L}{\omega}(\omega_o^2 - \omega^2)]} \quad (39)$$

Remember that  $N_A$  is the number of dipoles per unit area, an area density. The change in index of refraction can also be related to a volume density of dipoles,  $N_V$ , by the simple relation

$$N_A/\Delta z = N_V . \text{ Thus,}$$

$$n - 1 \approx \frac{N_V \mu_o \omega}{2} \frac{A_{\text{Loop}}^2}{[R + i \frac{L}{\omega} (\omega_o^2 - \omega^2)]} \quad (40)$$

The change in microwave index of refraction depends upon the volume density of scattering dipoles in exactly the same way that an optical index depends upon the density of atoms in a solid. Note that, for frequencies off resonance, the expression is a complex number, which indicates absorption effects.

Step 5: Estimating the Number of Waves of Phase Shift. Now consider some practical numbers for the phase shift. We would like to achieve a phase shift of up to  $2\pi$  radians, which is equivalent to a path length change of one wavelength:

$$(n - 1)\Delta z = \lambda .$$

From Eq. (39),

$$(n - 1)\Delta z = \frac{N_A \mu_o \omega}{2} \frac{A_{\text{Loop}}^2}{[R + i \frac{L}{\omega} (\omega_o^2 - \omega^2)]} \quad (41)$$

The largest effect occurs on resonance,  $\omega_0 = \omega$ . Assume that

$$f = 10 \text{ GHz} , \quad \omega = 2\pi \times 10^{10} \text{ s}^{-1} , \quad \lambda = 3 \text{ cm} = 3 \times 10^{-2} \text{ m} ,$$

$$A_{\text{Loop}} = 1 \text{ cm}^2 = 10^{-4} \text{ m}^2 ,$$

and suppose that the loops are 1 cm square and spaced on  $2/3 \lambda = 2 \text{ cm}$  spacings (Figure 35). This results in

$$N_A = 50 \times 50 \text{ m}^{-2} = 2.5 \times 10^3 \text{ m}^{-2} . \quad \text{With}$$

$$\mu_0 = 4\pi \times 10^{-7} \text{ V s/A m} \quad \text{and}$$

$$R = 1 \Omega = 1 \text{ V/A} \quad (\text{effectively a dielectric loss in C}) ,$$

$$(n-1)\Delta z = \frac{2.5 \times 10^3 \text{ m}^{-2} \times 4\pi \times 10^{-7} \text{ V s A}^{-1} \text{ m}^{-1} \times 2\pi \times 10^{10} \text{ s}^{-1} \times (10^{-4} \text{ m}^2)^2}{2 \times 1 \text{ V/A}}$$

$$\approx 1 \text{ m} .$$

17808-20

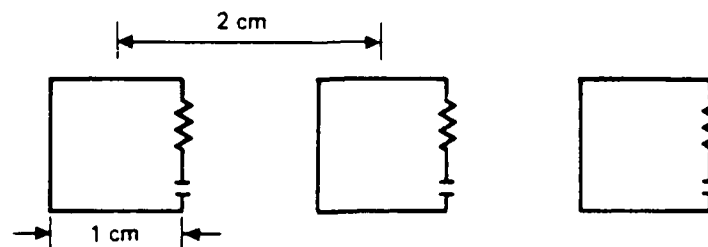


Figure 35. Resonant loop dimensions.

This result is large compared to one wavelength. We may conclude that the above assumptions that the dipole sheet will scatter only a small portion of the incident wave are incorrect. A more accurate estimate might be obtained by eliminating these small scattering approximations, but additional factors should also be included. For example, this calculation has neglected the effects of mutual coupling between adjacent resonant loops.

We conclude that a sheet of resonant loops can very strongly perturb the phase of an incident wave. A practical system may be able to use loops significantly smaller than those assumed above.

### 3.5.2 Magnetic Field Antennas

At frequencies above 1 GHz, the single-turn LRC resonator begins to resemble a wedding ring with a slot cut through it (Figure 36). In the limit of very small  $C$ , the loop approximates a dipole antenna. If the loop is straightened, the structure reduces to a simple half-wave dipole.

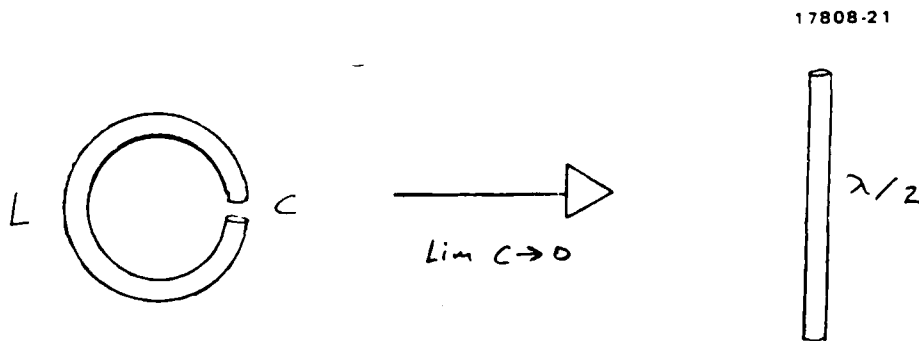


Figure 36. Single-turn resonator.

From this simple picture, it can be seen that the loop should have a circumference smaller than  $\lambda/2$ . As  $L$  is made smaller,  $C$  can be made larger for any given resonant frequency. Typically, ohmic and radiation losses in  $L$  are larger than dielectric losses in  $C$ . Thus, a reduction in  $L$  leads to a resonator with higher  $Q$  factor and a sharper resonance. The reduced area of the loop also couples less strongly to the surrounding electromagnetic fields, which may or may not be an advantage.

In principle, the inductance of a single-turn loop may be calculated from first principles. In practise, the result is a sensitive function of the diameter of the wire and the distribution of currents on the surface and within the volume of the wire.

The inductance of a small single loop can be determined by direct measurement (Radio Amateur's Handbook, 1979, p. 2-11). Consider a single-turn loop constructed of No. 12 bare wire (2.05 mm diameter) with a pitch of 8 turns per inch (a non-planar loop) and an inside diameter of 1/2 inch (1.27 cm). The measured inductance is  $4.5 \times 10^{-8}$  H. At a frequency of 10 GHz, this inductance could resonate with a capacitor of  $5.6 \times 10^{-3}$  pF, which is probably too small to be practical. Note also that the inside circumference of the loop is 3.99 cm, which is significantly longer than half of the 3-cm wavelength.

For a 10-GHz phase shifter, the loop must be smaller than 0.47 centimeter diameter to meet the  $\lambda/2$  criterion, which could be inconveniently small. However, there is another construction possibility. Dipole antennas are known to radiate well at their third harmonic frequencies, i.e., when their length is  $3\lambda/2$ . Resonant-loop antennas share this property.

In the older radio amateur literature, capacitively tuned resonant-loop antennas are known as VHF halo antennas (Figure 37), (Radio Amateur's Handbook, 1963, pp. 492-4). The resonant loop may be designed for a frequency of 1/3 of the

17808-23

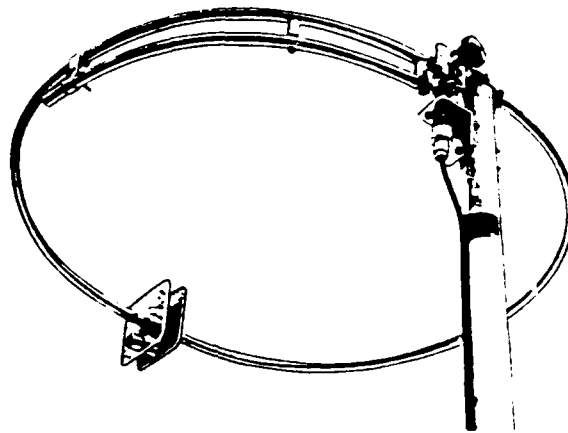


Figure 37. The 2-band halo antenna set up for 50-MHz operation; changing to 144 MHz involves decreasing the plate spacing and resetting the matching clip and series capacitor.

desired operating frequency. The circumference of the loop is typically about  $\lambda/3$  at the longer wavelength. A single capacitor can tune the resonance at either the fundamental or the third harmonic frequency.

A third-harmonic design for 10 GHz ( $\lambda = 3$  cm) would have the following dimensions:

Loop diameter  $d = 1$  cm.

Loop circumference = 3.14 cm

(approximately  $\lambda/3$  at the longer 9-cm wavelength).

Estimated inductance:  $L \approx 2.8 \times 10^{-8}$  H

Capacitance required to resonate at 3.3 GHz:

$C \approx 8.14 \times 10^{-14}$  F.

For a parallel-plate capacitor with plate spacing small compared to the plate diameter, the capacitance is given approximately by  $C = \epsilon_0 A/d$ , with  $\epsilon_0 = 8.83 \times 10^{-12}$  F/m. An air-spaced capacitor with square plates 1 mm on a side and spaced by 0.1 mm has a capacitance of approximately  $8.84 \times 10^{-14}$  F, which is just about right. Thus, a third-harmonic phase-shifter array might consist of 1-cm loops made from 1-mm diameter wire with a capacitor gap spacing of 0.1 mm.

### 3.5.3 Electric Field Antennas

As observed above, a resonant-loop antenna couples predominately to the magnetic field of an incident electromagnetic wave. A straight half-wave dipole couples to the electric field. An array of dipoles is similarly used to shift the phase of an incident wave transmission or reflection (Figure 38).

NO-A189 311

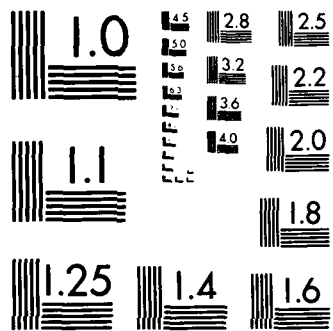
GROUND-BASED HIGH-POWER MICROWAVE DECOY DISCRIMINATION 2/2  
SYSTEM(U) HUGHES RESEARCH LABS MALIBU CA  
W O ECKHARDT ET AL 23 DEC 87 HAC-REF-G0656

UNCLASSIFIED

N00014-86-C-0878

F/G 19/12 NL





MICROCOPY RESOLUTION TEST CHART  
NATIONAL BUREAU OF STANDARDS-1963-A

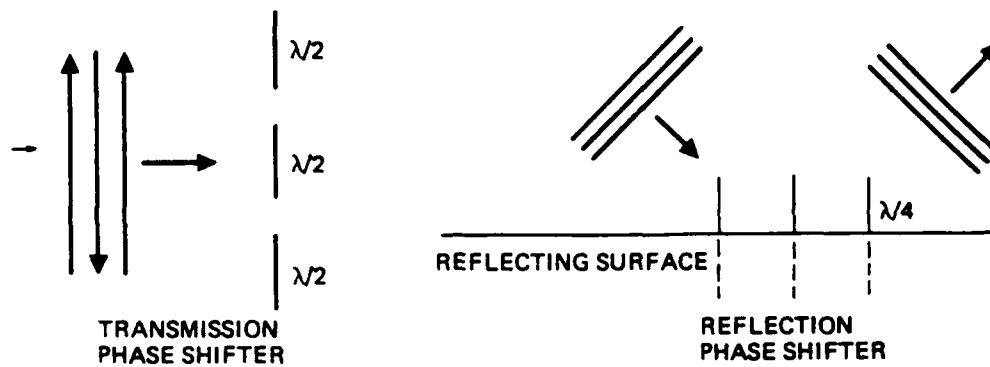


Figure 38. Dipole phase-shifter arrays.

In reflection, quarter-wave antenna elements may be deployed against a reflecting ground plane. Note that, at a conducting surface, the local electric field must be normal to the surface which is precisely optimal for coupling to these dipole arrays. A reflecting ground plane may be particularly convenient, since all control wires can be hidden behind the ground plane where they will not scatter the incident fields.

To achieve a variable phase shift, some method of tuning the dipoles through resonance must be found (Figure 39). It might consist of either capacitive or inductive loading at the center of the dipoles. Alternately, it may be feasible to digitally switch dipoles of various lengths to achieve above, at, or below resonance conditions.



Figure 39. Dipole tuning methods.

In the magnetic antenna case, it is straightforward to adjust the  $Q$  or sharpness of the resonance by changing the ratio of  $L$  to  $C$ . In general, heavily loaded antennas which are resonant but much smaller than the wavelength tend to have sharp resonances. Dipole antennas can be loaded with inductors and will exhibit similarly sharp resonances, but inductive loading is generally impractical at high frequencies. Some combination of switched stub tuning may provide both reasonably sharp resonances and convenient digital switching (Figure 40).

17808-27

#### DIGITALLY SWITCHED REFLECTING ARRAYS

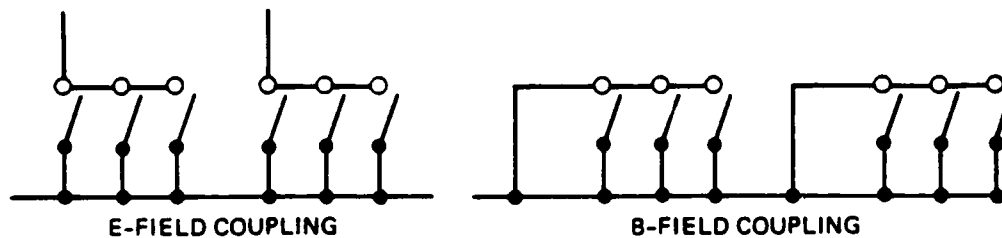


Figure 40. Digitally switched reflecting arrays.

## SECTION 4

### CONCLUSIONS

The effort this year has again resulted in a considerably increased understanding of the critical issues affecting the feasibility of the proposed ground-based HPM decoy discrimination system. We have shown that the predicted damage mechanism can be produced in high vacuum, and that the experiments agree with the predictions of our HPM/target interaction model. We have proposed a mechanism that might enable the production of measurable thrust reactions from decoys with much thicker metal coatings than what was previously thought to be feasible. We have established bounds on some important parameters of the antenna system, and potential solutions to the single most critical problem - the cost of the large phased-array antenna - have been identified.

Thus, the emphasis during the next year of performance will be on the theoretical and experimental study of HPM interactions with thick metal coatings and on feasibility demonstrations of the proposed phase-shifter approach.

## REFERENCES

1. D.O. Stringfellow, Calspan Secret Working Paper, 8th April, 1986, Doc. Control Log #0945961.
2. "CRO Handbook of Chemistry and Physics" 49th ed. Chemical Rubber Co., Ohio, 1969, p. D-33.
3. C. Kittel, "Introduction to Solid State Physics" Wiley & Sons, 1953, p. 130.
4. Ref. (2), p. E-10.
5. Ref. (3), p. 150.
6. "Machine Design", Vol. 59, No. 8, 150, (April, 1987).
7. M. Born & E. Wolf, "Principles of Optics" Pitman Press 1970.
8. J. Ready "Effects of High-Power Laser Radiation" Ac. Press (1971) p 107.
9. A. McDonald "Microwave Breakdown in Gases", Wiley & Sons, 1966, p. 69.
10. "Relation between the RF discharge parameters and plasma etch rates, selectivity and anisotropy", C.B. Zarowin, J. Vac. Sci. Technol. A2 1537 (1984).
11. "A theory of plasma-assisted chemical vapor transport processes", C.B. Zarowin, J. Appl. Phys. 57 929 (1985).
12. "Frequency effects in plasma etching", Daniel L. Flamm, J. Vac. Sci. Technol. A4 729 (1986).
13. "Plastic Insulating Materials", R.N. Sampson, in Standard Handbook for Electrical Engineers, D.G. Fink and J.M. Carroll, eds., Table 4-64 (McGraw-Hill, New York, 1968).
14. "Secondary Electron Emission", P.E. Best in Encyclopedia of Physics, R.G. Lerner and G.L. Trigg, eds., (Addison-Wesley, Reading, Massachusetts, 1981) p. 904.
15. "Electron and Ion Impact Phenomena", Edward W. Thomas ibid. p. 240.

16. "Ground-Based High-Power Microwave Decoy Discrimination System", Wilfried O. Eckhardt, Frank Chilton and James G. Small, Hughes Technical Summary, Report No. 1, Contract N00014-86-C-0878.
17. H. Brandt, A. Bromborsky, H. Burns, and R. Kens, "Microwave Generation in the Reflex Triode," Proc. 2nd Int. topical conf. on High-Power Electron and Ion-Beam Research and Technology, Cornell University, Ithaca, New York, 649 (1977).
18. M. Read, R. Seeley and W. Manheimer, IEEE Trans. Plasma Sci., PS-13, 398 (1985).
19. L. Ives, M. Caplan, H. Huey, "High Pulsed Power Microwave Source Studies", Proc., 3rd Natl. Conf. on High Power Microwave Technology for Defense Applications, Albuquerque, NM, Dec. (1986).
20. J. Clark, T. Orzechowski and S. Yarema, "An Efficient High Power Microwave Source at 35 GHz Using an Induction Linac Free Electron Accelerator", Proc., 3rd Natl. Conf. on High Power Microwave Technology for Defense Applications, Albuquerque, NM, Dec. (1986).

ENVD

DÄTE

3-88

DTIC